



Generalized pyrolysis model for combustible solids

Chris Lautenberger*, Carlos Fernandez-Pello

Department of Mechanical Engineering, University of California, Berkeley, CA 94720, USA

ARTICLE INFO

Article history:

Received 13 November 2007

Received in revised form

18 March 2009

Accepted 20 March 2009

Available online 20 May 2009

Keywords:

Pyrolysis

Charring

Intumescence

Material properties

Genetic algorithms

ABSTRACT

This paper presents a generalized pyrolysis model that can be used to simulate the gasification of a variety of combustible solids encountered in fires. The model, Gpyro, can be applied to noncharring polymers, charring solids, intumescent coatings, and smolder in porous media. Temperature, species, and pressure distributions inside a thermally stimulated solid are determined by solving conservation equations for the gaseous and condensed phases. Diffusion of species from the ambient into the solid is calculated with a convective–diffusive solver, providing the capability to calculate the flux and composition of volatiles escaping from the solid. To aid in determining the required material properties, Gpyro is coupled to a genetic algorithm that can be used to estimate the model input parameters from bench-scale fire tests or thermogravimetric (TG) analysis. Model calculations are compared to experimental data for the thermo-oxidative decomposition of a noncharring solid (PMMA), thermal pyrolysis of a charring solid (white pine), gasification and swelling of an intumescent coating, and smolder in polyurethane foam. Agreement between model calculations and experimental data is favorable, especially when one considers the complexity of the problems simulated.

© 2009 Elsevier Ltd. All rights reserved.

1. Introduction

One of the most promising long-term goals of fire research is prediction of large-scale fire development with computer modeling. This involves coupling a gas phase model that handles fluid mechanics, heat/mass transfer, and combustion to a condensed phase model that simulates the heating and gasification (pyrolysis) of thermally stimulated combustibles. Although pyrolysis modeling has received considerable attention from the fire community, with no fewer than eight reviews having been published since 1993 [1–8], it is rare for a pyrolysis model to be applied outside of the research environment in which it was developed. The primary reasons for this are twofold: (1) it is difficult to determine the model input parameters (or “material properties”) required to characterize practical combustibles, and (2) pyrolysis models have traditionally been formulated in a way that makes them applicable only to one particular class of materials (e.g., noncharring [9], charring [10], intumescent [11], or smolder in porous media [12]) thereby limiting their applicability to fire problems where a range of fuels are encountered.

With these two barriers in mind, this paper presents the formulation of Gpyro [13], an open-source generalized pyrolysis model that is capable of simulating the pyrolysis of a variety of materials. Gpyro is coupled to a material property estimation algorithm that can be used to estimate model input parameters

from thermogravimetric (TG) analysis and bench-scale flammability tests such as the cone calorimeter.

Rather than developing separate sets of model equations for charring, noncharring, intumescent, or smoldering materials, Gpyro is formulated from general conservation laws. A particular material is simulated by specifying a set of model input parameters (thermophysical properties, reaction mechanisms, etc.), sometimes referred to as “material properties”. Similarly, a particular experimental configuration or fire scenario is simulated through specification of initial and boundary conditions. The flexibility to invoke or omit submodels is provided because there may be little consequence to omitting a particular phenomenon other than reducing the computational expense and the number of parameters that must be specified. Gpyro source code, binaries, sample input files, a user's guide, and a technical reference guide are available electronically [13]. Background information is provided in the Ph.D. Dissertation of Lautenberger [14].

In this paper, the mathematical formulation of Gpyro is presented in Sections 2–5. In Section 6, Gpyro simulations of several different experiments are presented: (1) thermo-oxidative decomposition of a noncharring thermoplastic (PMMA); (2) anaerobic pyrolysis of a charring material (white pine); (3) gasification and swelling of an intumescent coating; and (4) propagation of a smolder wave in polyurethane foam.

Although Section 6 includes a comparison of Gpyro calculations to experimental data, it is emphasized that these simulations are presented primarily to demonstrate the types of problems that can be analyzed with Gpyro, rather than to “validate” it for any particular material or configuration.

* Corresponding author. Tel.: +1510 643 0178; fax: +1510 642 1850.

E-mail address: clauten@me.berkeley.edu (C. Lautenberger).

| Nomenclature | | ε | emissivity |
|----------------------|--|---------------------|---|
| <i>Letters</i> | | κ | radiative absorption coefficient |
| A | condensed phase species A (reactant) | ν | viscosity (μ/ρ) or reaction stoichiometry coefficient (Eq. (20)) |
| B | condensed phase species B (product) | ρ | density |
| c | specific heat capacity | χ | fraction of density difference realized as gases |
| E | activation energy | τ | dummy variable of integration |
| h | enthalpy | ψ | porosity |
| h_c | convective heat transfer coefficient | $\dot{\omega}''$ | reaction rate |
| \dot{j} | diffusive mass flux | <i>Subscripts</i> | |
| k | thermal conductivity (Eq. (6)) | 0 | initial |
| K | permeability or number of reactions | ∞ | ambient |
| \dot{m}'' | mass flux | b | interface between point cell and bottom cell |
| M | molecular weight or number of condensed phase species | B | bottom cell |
| N | number of gaseous species | d | destruction |
| n | exponent (reaction order, O ₂ sensitivity, property temperature dependence) | e | external |
| P | pressure | f | formation |
| \dot{q}'' | heat flux | g | gas |
| \dot{Q}''' | heat generation per unit volume | i | condensed phase species i |
| R | universal gas constant | j | gaseous species j |
| SF | solid fraction (see Eq. (21)) | k | reaction index |
| t | time | nb | no blowing |
| T | temperature | P | point cell |
| X | volume fraction | r | radiative (Eq. (6)) or reference (Eq. (1)) |
| y | yield | s | solid |
| Y | mass fraction | t | interface between point cell and top cell |
| z | distance | T | top cell |
| Z | pre-exponential factor | ν | volatiles |
| Δz | grid size | Σ | see Eq. (33) |
| <i>Greek symbols</i> | | <i>Superscripts</i> | |
| γ | radiative conductivity parameter (see Eq. (6)) | \circ | at time t |
| δ | thickness or Kronecker delta | | |

The reason for this is that pyrolysis model validation is intimately connected to material property estimation. Since the simulations presented here require specification of several model input parameters that cannot be directly measured in the laboratory, genetic algorithm optimization [15,16] is used to estimate the required model parameters from flammability test data and thermogravimetric analysis.

2. Preliminaries, properties, and definitions

Gpyro considers a condensed phase combustible material that is composed of M chemically distinct condensed phase species. Condensed phase species could be pure polymer, glass fiber reinforcements, char, ash, etc. Within a material, the initial concentrations of each species may be uniform (as in the case of a homogeneous composite) or vary spatially (as in the case of laminated composites and wood). This is referred to as the material's microstructure. As the solid is heated, it degrades to form N chemically distinct gaseous species including hydrocarbon fragments, water vapor, carbon monoxide, etc. Gaseous species may be consumed or produced by both heterogeneous (solid/gas) reactions and homogeneous (gas/gas) reactions.

Since the condensed and gaseous phases are, respectively, composed of M and N chemically distinct species with different thermophysical properties, effective properties appearing in the

conservation equations presented later must be calculated from appropriately weighted (mass or volume fraction) local compositions. Weighted quantities are denoted with an overbar ($\bar{\phi}$). Throughout this work, Y_i is the mass of condensed phase species i divided by the total mass of all condensed phase species, and Y_j is the mass of gaseous species j divided by the mass of all gaseous species.

Thermophysical properties (k , ρ , and c) of each condensed phase species are assumed to vary with temperature as $\phi(T) = \phi_0(T/T_r)^{n_\phi}$, where ϕ_0 and n_ϕ are user-specified parameters and T_r is a user-specified reference temperature often (but not necessarily) taken as 300 K. Thus, Gpyro can accommodate general trends such as an increase in c with temperature. However, detailed temperature dependencies of the underlying thermophysical properties cannot be included. This is not necessarily a drawback because rarely are accurate temperature-dependent measurements of $k(T)$, $c(T)$, or $\rho(T)$ available, particularly at temperatures above 300 °C that are relevant to burning, or for intermediate species such as char or ash. It is felt that for a generalized pyrolysis model, the simplicity of a two-parameter approximation for thermophysical properties outweighs any potential drawbacks associated with the inability to specify detailed temperature-dependent properties. Furthermore, review of the literature on thermal properties for polymers and wood (e.g., Ref. [14]) shows that specific heat capacity and thermal conductivity often exhibit a smooth, monotonic variation with

temperature that can be well approximated by $\phi(T) = \phi_0(T/T_r)^{n_\phi}$. Thermal properties of polymers often exhibit a “jump” at the glass transition or melting point, which can be modeled in Gpyro with a solid–solid reaction that occurs at a specified temperature.

2.1. Bulk density

The bulk density of each condensed phase species varies with temperature according to the relation:

$$\rho_i(T) = \rho_{0,i} \left(\frac{T}{T_r} \right)^{n_{\rho,i}} \quad (1)$$

where $\rho_{0,i}$ and $n_{\rho,i}$ are user-specified parameters. Here, ρ_i is the bulk density (total mass divided by total volume) of species i under vacuum. This nomenclature is different from other pyrolysis models where ρ_i is the mass of species i per unit volume of mixture (which would instead be denoted here as $\bar{\rho}Y_i$).

The weighted bulk density under vacuum can be calculated from either condensed phase mass or volume fractions:

$$\bar{\rho} = \sum_{i=1}^M X_i \rho_i \quad (2)$$

$$\bar{\rho} = \left(\sum_{i=1}^M \frac{Y_i}{\rho_i} \right)^{-1} \quad (3)$$

2.2. Porosity

It is assumed that porosity (ψ) is a property of each condensed phase species, where ψ_i is calculated as follows:

$$\psi_i(T) = 1 - \frac{\rho_i(T)}{\rho_{s0,i}} \quad (4)$$

$\rho_{s0,i}$ is a user-specified constant corresponding to the “solid density” (density of a material in its nonporous form) of species i at a particular temperature. Assuming that porosity is a property of each condensed phase species eliminates the need to solve a separate porosity evolution equation because the weighted porosity can be calculated from the local composition as

$$\bar{\psi} = \sum X_i \psi_i \quad (5)$$

2.3. Effective thermal conductivity

Effective thermal conductivity of each condensed phase species is broken into a solid and a radiative component:

$$k_i(T) = k_{0,i} \left(\frac{T}{T_r} \right)^{n_{k,i}} + \gamma_i \sigma T^3 \quad (6)$$

The second term on the RHS of Eq. (6) is attributed to radiation heat transfer across pores, which may become dominant mode of heat transfer in porous media at high temperatures. γ_i is an empirical parameter (with units of length) that depends on pore morphology and other considerations.

The effective thermal conductivity specified by setting $k_{0,i}$, $n_{k,i}$, and γ_i in Eq. (6) should take into account bulk density, moisture content, porosity, microstructure, grain orientation, and any other factors affecting thermal conductivity. This is commensurate with the spirit of the present work, which aims to formulate a generalized model and code the governing equations in a self-consistent manner rather than consider detailed submodels for thermophysical properties of specific materials.

As with bulk density and porosity, the averaged effective thermal conductivity is weighted by condensed phase volume fractions:

$$\bar{k} = \sum_{i=1}^M X_i k_i \quad (7)$$

It is recognized that for some materials, effective thermal conductivity may not be proportional to component volume fraction (Eq. (7)) and a more complex model for effective thermal conductivity may be justified. However, Eq. (7) should be a good approximation for many materials encountered in fires.

2.4. Apparent specific heat capacity and sensible enthalpy

Temperature-dependent specific heat capacity of species i is calculated as

$$c_i(T) = c_{0,i} \left(\frac{T}{T_r} \right)^{n_{c,i}} \quad (8)$$

The sensible enthalpy of condensed phase species i at temperature T is determined by integrating Eq. (8):

$$h_i(T) = \int_{T_d}^T c(\theta) d\theta = \frac{c_{0,i}}{n_{c,i} + 1} \left(T \left(\frac{T}{T_r} \right)^{n_{c,i}} - T_d \left(\frac{T_d}{T_r} \right)^{n_{c,i}} \right) \quad (9)$$

where T_d is the temperature datum used to establish an absolute value of enthalpy (taken as 200 K).

Specific heat capacity and sensible enthalpy are weighted by condensed phase mass fractions:

$$\bar{c} = \sum_{i=1}^M Y_i c_i \quad (10)$$

$$\bar{h} = \sum_{i=1}^M Y_i h_i \quad (11)$$

2.5. Radiative properties

The user must also specify for each condensed phase species an emissivity (ε_i , dimensionless) and radiative absorption coefficient (κ_i , m^{-1}). Emissivity controls the fraction of the incident radiation absorbed at the surface and the fraction of the surface blackbody emissive power that is radiated away. The radiative absorption coefficient controls the depth over which incident thermal radiation is attenuated. Averaged radiative properties are weighted by volume:

$$\bar{\varepsilon} = \sum_{i=1}^M X_i \varepsilon_i \quad (12)$$

$$\bar{\kappa} = \sum_{i=1}^M X_i \kappa_i \quad (13)$$

2.6. Permeability

Each condensed phase species must be assigned a permeability (m^2). The averaged permeability is weighted by volume:

$$\bar{K} = \sum_{i=1}^M X_i K_i \quad (14)$$

2.7. Gas density and molecular weight

In addition to condensed phase properties, several gas phase properties are required. The gas phase density is calculated from

the ideal gas law:

$$\rho_g = \frac{P\bar{M}}{RT_g} \quad (15)$$

In Eq. (15), R is the universal gas constant, and the mean molecular mass (\bar{M}) is calculated from the local volume fractions of all gaseous species:

$$\bar{M} = \sum_{j=1}^N X_j M_j \quad (16)$$

2.8. Gaseous specific heat capacity and enthalpy

All gaseous species are assumed to have equal specific heat capacities that are independent of temperature. This approximation is justified given that little is known about the actual composition of the gaseous volatiles produced during the pyrolysis and gasification of practical materials. As with condensed phase enthalpy, gas phase sensible enthalpy is weighted by mass:

$$\bar{h}_g = \sum_{j=1}^N Y_j h_{g,j} = c_{pg}(T_g - T_d) \quad (17)$$

where c_{pg} denotes the (constant) gaseous specific heat capacity.

2.9. Gaseous mass diffusivity, thermal conductivity, and viscosity

Gaseous diffusion coefficients are calculated from Chapman–Enskog theory. The binary diffusion coefficient (units of m^2/s) for species A diffusing into species B is

$$D_{AB} = 0.018829 \frac{\sqrt{T^3 \left(\frac{1}{M_A} + \frac{1}{M_B} \right)}}{P \sigma_{AB}^2 \Omega_{D,AB}} \quad (18a)$$

In Eq. (18a), M_A and M_B have units of g/mol , σ_{AB} is a weighted collision diameter of species A and B (units of \AA), k_b is the Boltzmann constant, and ε_{AB} is the maximum energy of attraction between molecules A and B . Thus, σ_{AB} and $(\varepsilon/k_b)_{AB}$ are model parameters that describe the binary diffusion coefficient of species A into species B . These parameters are tabulated for several gases by Bird et al. [17], along with $\Omega_{D,AB}$ as a function of $T/(\varepsilon_{AB}/k_b)$. Note that σ_{AB} and ε_{AB} are weighted averages between molecules A and B :

$$\sigma_{AB} = \frac{1}{2}(\sigma_A + \sigma_B) \quad (18b)$$

$$\varepsilon_{AB} = \sqrt{\varepsilon_A \varepsilon_B} \quad (18c)$$

Since little is known about the composition of gaseous volatiles for practical materials, several approximations are made to simplify the gas phase calculations. It is assumed that all gaseous species have the same diffusivity ($D_{AB} = D$), taken as that of oxygen into the (user-specified) background species. Unit Prandtl, Schmidt, and Lewis numbers are assumed ($\text{Pr} = \text{Sc} = 1$). It follows from these approximations:

$$k_g \approx \rho_g D c_{pg} \quad (19a)$$

$$\nu \approx D \quad (19b)$$

Eq. (19a) allows for considerable simplification of the gas phase energy equation (see the Gpyro technical reference [13]).

3. Reaction rates and source terms

In Gpyro, two types of reactions are considered: heterogeneous (solid/gas) and homogeneous (gas/gas). Heterogeneous reactions

involve the destruction of a condensed phase species to form gases and/or additional condensed phase species. An example is char formation wherein one condensed phase species (e.g., wood) is converted to a second condensed phase species (e.g., char) with the release of gases (e.g., pyrolysate). Heterogeneous reactions may also involve the consumption of gases. Homogeneous gas phase reactions, such as the oxidation of gaseous pyrolysate in the pore space, involve only gases.

3.1. Heterogeneous reaction stoichiometry

A particular condensed phase reaction is denoted by the index k , and the total number of condensed phase reactions is designated K (not to be confused with permeability; it should be clear from context which is meant). In the combustion literature, stoichiometry of gas phase reactions is often expressed using molar “ ν ” coefficients. The same is done here, with the important difference that the ν coefficients are defined on a mass basis. General heterogeneous reactions are represented in Gpyro as

$$1 \text{ kg } A_k + \sum_{j=1}^N \nu'_{j,k} \text{ kg gas } j \rightarrow \nu_{B,k} \text{ kg } B_k + \sum_{j=1}^N \nu''_{j,k} \text{ kg gas } j \quad (20a)$$

$$\nu_{B,k} = \text{SF}_k \quad (20b)$$

$$\nu'_{j,k} = -(1 - \text{SF}_k) \min(y_{s,j,k}, 0) \quad (20c)$$

$$\nu''_{j,k} = (1 - \text{SF}_k) \max(y_{s,j,k}, 0) \quad (20d)$$

A_k denotes the condensed phase reactant species and B_k denotes the condensed phase product species. The composition of the gases consumed and produced by a heterogeneous reaction is controlled by the parameters $\nu'_{j,k}$ and $\nu''_{j,k}$. In Eq. (20a), $\nu'_{j,k}$ is the net mass of gaseous species j consumed by reaction k , and $\nu''_{j,k}$ is the net mass of gaseous species j produced by reaction k per unit mass of A_k consumed.

A user-defined “species yield matrix” is introduced to generalize the specification of $\nu'_{j,k}$ and $\nu''_{j,k}$. This N by K matrix, denoted $y_{s,j,k}$, appears on the RHS of Eqs. (20c) and (20d). The entries of $y_{s,j,k}$ may be positive or negative, with a positive entry corresponding to net production of a gaseous species by a particular reaction, and a negative entry corresponding to net consumption of a gaseous species by a particular reaction. The physical meaning of each entry in the species yield matrix is the net mass of gas phase species j consumed or generated by reaction k per unit mass of condensed phase that is converted to gases by reaction k .

The ν coefficients are related to the “solid fraction” (SF) of reaction k , denoted SF_k . The solid fraction of reaction k is the fraction of condensed phase species A_k ’s mass that is converted to condensed phase species B_k . The solid fraction is related to the bulk densities of condensed phase reactant and product species A_k and B_k as:

$$\text{SF}_k = 1 + \left(\frac{\rho_{B_k}}{\rho_{A_k}} - 1 \right) \chi_k \quad (21)$$

Since bulk densities may depend on temperature, SF_k may be a function of temperature. In Eq. (21), the parameter χ_k is the fraction of the bulk density difference between condensed phase species A_k and B_k that is converted to gases (discussed in Section 3.3).

3.2. Heterogeneous reactions—volumetric source terms

In Section 3.3, kinetics considerations are used to develop an expression for $\dot{\omega}'''_{dA_k}$, the local volumetric destruction rate of condensed phase reactant A_k . In Gpyro, local volumetric formation

or destruction rates of all other condensed/gaseous species by heterogeneous reactions are related to $\dot{\omega}_{dA_k}'''$ via the stoichiometry presented in Section 3.1.

The formation rate of condensed phase species B_k by reaction k ($\dot{\omega}_{B_k}'''$) and the rate at which the mass of condensed phase species A_k is volatilized or converted to gases by reaction k ($\dot{\omega}_{fA_k}'''$) are calculated from

$$\dot{\omega}_{B_k}''' = \text{SF}_k \dot{\omega}_{dA_k}''' = \left(1 + \left(\frac{\rho_{B_k}}{\rho_{A_k}} - 1\right) \chi_k\right) \dot{\omega}_{dA_k}''' \quad (22)$$

$$\dot{\omega}_{fA_k}''' = (1 - \text{SF}_k) \dot{\omega}_{dA_k}''' = \left(1 - \frac{\rho_{B_k}}{\rho_{A_k}}\right) \chi_k \dot{\omega}_{dA_k}''' \quad (23)$$

Eq. (23) gives $\dot{\omega}_{fA_k}'''$, the formation rate of *all* gases by reaction k . However, it does not provide any information regarding the production/destruction rates of *individual* gaseous species. This information is provided via the user-specified species yield matrix $y_{s,j,k}$ mentioned earlier:

$$\dot{\omega}_{s,fj,k}''' = \dot{\omega}_{fA_k}''' \max(y_{s,j,k}, 0) \quad (24)$$

$$\dot{\omega}_{s,dj,k}''' = -\dot{\omega}_{fA_k}''' \min(y_{s,j,k}, 0) \quad (25)$$

Here, the subscript s stands for “solid” as a reminder that gaseous species may also be formed or destroyed by homogeneous gas phase reactions.

These volumetric source terms apply to a single reaction k . However, the conservation equations presented later contain total source terms that are obtained by summing over all reactions. The total formation rate of all gases by volatilization of the condensed phase ($\dot{\omega}_{fg}'''$) is calculated by summing Eq. (23) over all condensed phase reactions, and the total destruction and formation rates of gases due to heterogeneous reactions are calculated by summing over Eqs. (24) and (25):

$$\dot{\omega}_{fg}''' = \sum_{k=1}^K \dot{\omega}_{fA_k}''' \quad (26)$$

$$\dot{\omega}_{s,dj}''' = \sum_{k=1}^K \dot{\omega}_{s,dj,k}''' \quad (27)$$

$$\dot{\omega}_{s,fj}''' = \sum_{k=1}^K \dot{\omega}_{s,fj,k}''' \quad (28)$$

The total destruction rate of condensed phase species i and the total formation rate of condensed phase species i are calculated as

$$\dot{\omega}_{di}''' = \sum_{k=1}^K \delta_{i,A_k} \dot{\omega}_{dA_k}''' \quad (29)$$

$$\dot{\omega}_{fi}''' = \sum_{k=1}^K \delta_{i,B_k} \dot{\omega}_{fB_k}''' \quad (30)$$

In Eqs. (29) and (30), δ is the Kronecker delta, which has the properties for general indices i and j :

$$\delta_{ij} = \begin{cases} 1 & \text{if } i = j \\ 0 & \text{if } i \neq j \end{cases} \quad (31)$$

In Eq. (31), i and j , do not represent condensed and gaseous species as is convention elsewhere.

3.3. Heterogeneous reactions—noncharring, charring, and intumescent

In a noncharring reaction, condensed phase reactant species A_k is transformed completely to product gases, forming no

condensed phase residue. This type of reaction is invoked in Gpyro by setting $\chi_k = 1$ and specifying no condensed phase product species B_k . It can be seen from Eq. (22) that SF_k becomes zero if $\rho_{B_k} = 0$ and $\chi_k = 1$. Consequently, the formation rate of condensed phase species B_k is also zero. At the same time, the quantity $1 - \text{SF}_k$ in Eq. (23) becomes 1, meaning that only gases are generated. Mass conservation requires a noncharring reaction to cause surface regression.

For charring and intumescent reactions, the degree of shrinkage or swelling is controlled by the parameters χ_k , ρ_{A_k} , and ρ_{B_k} . Different values of these parameters can be used to simulate charring reactions that result in no net volume change, charring reactions where swelling occurs (intumescence), charring reactions where shrinkage occurs, and condensation reactions where gas phase mass is converted to condensed phase mass.

If $\chi_k = 1$ and $0 < \rho_{B_k} < \rho_{A_k}$, a charring reaction with no volume change occurs. From Eqs. (22) and (23), the formation rate of condensed phase species B and gases are both nonzero.

Eqs. (22) and (23) can also be used to model an intumescent reaction with swelling by setting $0 \leq \chi_k < 1$. Provided $\rho_{B_k} < \rho_{A_k}$, a lower density solid is formed from a higher density solid and swelling occurs to conserve mass. In the extreme case $\chi_k = 0$, swelling occurs without any escape of gases. Values of χ_k between 0 and 1 cause intumescence (swelling) to occur simultaneously with the release of gaseous vapors, with the relative amounts of swelling and volatilization dictated by the value of χ_k .

Values of χ_k between 1 and $\rho_{A,k}/(\rho_{A,k} - \rho_{B,k})$ can be used to simulate a charring reaction that results in shrinkage (provided $\rho_{B_k} < \rho_{A_k}$). Essentially, the decreased formation rate of condensed phase species B_k (see Eq. (22) and note that the term in parentheses is negative) caused by a value of χ_k greater than 1 leads to a decrease in the local grid size through the condensed phase mass conservation equation.

Finally, values of χ_k greater than $\rho_{A,k}/(\rho_{A,k} - \rho_{B,k})$ can be used to simulate condensation reactions where gas phase mass is converted to condensed phase mass.

The preceding discussion applies to cases where $\rho_{B_k} < \rho_{A_k}$ (a lower density solid is formed from a higher density solid). However, the case where $\rho_{B_k} > \rho_{A_k}$ is also conceivable, and the behavior is the opposite of intumescence. If $\chi_k = 0$, then shrinkage would occur with no change in mass. This could be used to model a porous material that melts or collapses when heated. If $\chi_k = 1$, then no volume change would occur, but an increase in mass would occur (negative mass loss rate). For $0 < \chi_k < 1$, shrinkage would occur simultaneously with mass gain, with the relative amounts of shrinkage and mass gain dictated by the value of χ_k .

3.4. Heterogeneous reaction kinetics

Pyrolysis reaction stoichiometry and calculation of analogous volumetric source terms are described above, but the rate at which reactions occur (kinetics) must also be quantified. First, define α_i as the conversion of condensed phase species i . Note that conversion is related to instantaneous mass (m) and initial mass (m_0) as $\alpha = 1 - m/m_0$. Since conversion is tracked locally in each cell, $1 - \alpha_i$ is calculated in a grid cell having size Δz as

$$1 - \alpha_i = \frac{m_i'}{m_{i,\Sigma}'} = \frac{\bar{\rho} Y_i \Delta z}{(\bar{\rho} Y_i \Delta z)_{\Sigma}} \quad (32)$$

In Eq. (32), the numerator is the mass per unit area of condensed phase species i in a particular cell; the denominator is the initial (i.e., at $t = 0$) mass per unit area of condensed phase species i in that same cell plus the cumulative formation of

species i through time t in that cell:

$$(\bar{\rho}Y_i\Delta z)_\Sigma \equiv (\bar{\rho}Y_i\Delta z)|_{t=0} + \int_0^t \dot{\omega}_{fi}'''(\tau)\Delta z(\tau)d\tau \quad (33)$$

The subscript Σ serves as a reminder that $(\bar{\rho}Y_i\Delta z)_\Sigma$ includes an integral. Note that $\dot{\omega}_{fi}''' \geq 0$ because $\dot{\omega}_{fi}'''$ is the formation rate of condensed phase species i .

The k th reaction rate is the destruction rate of condensed phase species A_k by condensed phase reaction k ($\dot{\omega}_{dA_k}'''$). For each reaction k , the index of the condensed phase reactant species (A_k) and the index of the condensed phase product species (B_k) are user-specified. The heterogeneous reaction rate is calculated as

$$\dot{\omega}_{dA_k}''' = f(\alpha_{A_k}) \frac{(\bar{\rho}Y_{A_k}\Delta z)_\Sigma}{\Delta z} Z_k \exp\left(-\frac{E_k}{RT}\right) \times g(Y_{O_2})H(T - T_{crit,k}) \quad (34a)$$

$$f(\alpha_{A_k}) = (1 - \alpha_{A_k})^{n_k} = \left(\frac{\bar{\rho}Y_{A_k}\Delta z}{(\bar{\rho}Y_{A_k}\Delta z)_\Sigma} \right)^{n_k} \quad (34b)$$

The reaction model is $f(\alpha_{A_k})$, assumed in this paper to be n th order per Eq. (34b). Alternate reaction model options are discussed in the Gpyro technical reference [13]. $H(T - T_{crit,k})$ is the Heaviside step function, forcing the reaction rate to be zero below $T_{crit,k}$. The function $g(Y_{O_2})$ in Eq. (34) is calculated as

$$g(Y_{O_2}) = \begin{cases} 1 & \text{for } n_{O_2,k} = 0 \\ (1 + Y_{O_2})^{n_{O_2,k}} - 1 & \text{for } n_{O_2,k} \neq 0 \end{cases} \quad (35)$$

An alternate form of $g(Y_{O_2})$ that is not used in this paper is presented in the Gpyro technical reference [13]. In Eq. (35), the oxygen mass fraction (Y_{O_2}) is the local value inside the decomposing solid as determined by solution of the gaseous species conservation equations (except for TGA simulations where it is taken as the freestream value). The exponent $n_{O_2,k}$ describes the oxygen sensitivity of reaction k , so a value of $n_{O_2,k} = 0$ is specified for reactions that are not sensitive to oxygen.

3.5. Heat release/absorption due to heterogeneous reactions

In Gpyro, the total heat of reaction is calculated as the sum of two separate contributions. One part of the heat of reaction applies only to the generation of condensed phase species and is denoted $\Delta H_{sol,k}$ (where *sol* stands for *solid*). The other part applies only to the generation of volatiles from the condensed phase and is denoted $\Delta H_{vol,k}$ (where *vol* stands for *volatiles*). The volumetric rate of heat release or absorption to the solid phase due to reaction k is

$$\dot{Q}_{s,k}''' = \begin{cases} -\dot{\omega}_{fB_k}''' \Delta H_{sol,k} - \dot{\omega}_{fB_k}''' \Delta H_{vol,k} & \text{for } \Delta H_{sol,k} \neq \Delta H_{vol,k} \\ -\dot{\omega}_{dA_k}''' \Delta H_k & \text{for } \Delta H_{sol,k} = \Delta H_{vol,k} = \Delta H_k \end{cases} \quad (36)$$

$\Delta H_{sol,k}$ is the user-specified chemical (not sensible) specific enthalpy difference between condensed phase species B_k and A_k , i.e. $\Delta H_{sol,k} = h_{B_k}^\circ - h_{A_k}^\circ$ where “ $^\circ$ ” denotes chemical enthalpy. The units of $\Delta H_{sol,k}$ are Joules per kilogram of species B_k produced by reaction k .

$\Delta H_{vol,k}$ is the user-specified quantity of energy required to convert unit mass of condensed phase species A_k to gases at whatever temperature the reaction occurs. $\Delta H_{vol,k}$ is treated here as a user-specified empirical constant because detailed knowledge of the chemical and sensible enthalpies of all gaseous and condensed phase species is required to assign physical/chemical significance to $\Delta H_{vol,k}$. The units of $\Delta H_{vol,k}$ are Joules per kilogram of gases volatilized from condensed phase species A_k . $\Delta H_{vol,k}$ is sometimes called the heat of pyrolysis, heat of volatilization, or

heat of vaporization. It is different from the heat of gasification (sometimes denoted ΔH_g or L_g), which includes a contribution for the sensible enthalpy required to heat the condensed phase from its initial temperature to its volatilization temperature.

Heats of reaction are sometimes given on a Joules per kilogram of *reactant consumed* basis. This treatment can be recovered in Gpyro by setting $\Delta H_{sol,k} = \Delta H_{vol,k} = \Delta H_k$. In fact, the second equality in Eq. (36) follows from the first equality after setting $\Delta H_{sol,k} = \Delta H_{vol,k} = \Delta H_k$ and then making use of the relation $\dot{\omega}_{fB_k}''' + \dot{\omega}_{fB_k}''' = \dot{\omega}_{dA_k}'''$. The flexibility that this affords is the primary motivation for splitting the heat of reaction into two separate components.

Positive values of $\Delta H_{sol,k}$ or $\Delta H_{vol,k}$ correspond to an endothermic reaction, and negative values correspond to an exothermic reaction.

3.6. Homogeneous gas phase reactions

In addition to heterogeneous reactions involving condensed and gaseous phases, the user may also specify any number of homogeneous gas phase reactions that occur inside the pore space. Just as there are K condensed phase reactions and individual condensed phase reactions are indicated by the index k , there are L homogeneous gas phase reactions, and individual reactions are indicated by the index ℓ . Each homogeneous gas phase reaction ℓ converts two gas phase reactants (A_ℓ and B_ℓ) to gaseous products.

Stoichiometry of homogeneous gas phase reactions is expressed on a mass basis:

$$1 \text{ kg } A_\ell - y_{g,B_\ell,\ell} \text{ kg } B_\ell \rightarrow \sum_{j=1}^N \max(y_{g,j,\ell}, 0) \text{ kg gas } j \quad (37)$$

In Eq. (37), $y_{g,j,\ell}$ is the N by L “homogeneous gaseous species yield matrix”, analogous to the gaseous species yield matrix ($y_{s,j,k}$) discussed earlier with reference to heterogeneous reactions. The physical meaning of individual entries in $y_{g,j,\ell}$ is the net mass of gaseous species j produced by reaction ℓ (for positive entries) or consumed by reaction ℓ (for negative entries) per unit mass of gaseous species A_ℓ consumed. Note that in writing Eq. (37), it is assumed that $y_{g,A_\ell,\ell} = -1$, i.e. the yield corresponding to gas phase species A_ℓ is -1 . It is also assumed that for reaction ℓ , the only other negative entry in the $y_{g,j,\ell}$ matrix is the yield corresponding to gas phase species B_ℓ (denoted $y_{g,B_\ell,\ell}$ in Eq. (37)). This is why there is a negative sign in front of the second term on the LHS of Eq. (37).

The reaction rate of the ℓ th homogeneous gas phase reaction is the destruction rate of gas phase species A_ℓ :

$$\dot{\omega}_{dA_\ell}''' = [A_\ell]^{p_\ell} [B_\ell]^{q_\ell} T^{b_\ell} \bar{\nu}_\ell \exp\left(-\frac{E_\ell}{RT_g}\right) \quad (38)$$

In Eq. (38), $\dot{\omega}_{dA_\ell}'''$ is the destruction rate of gaseous species A_ℓ due to homogeneous gas phase reaction ℓ , and $[A_\ell]$ denotes the molar concentration of gaseous species A_ℓ :

$$[A_\ell] = \frac{\rho_g Y_{A_\ell}}{M_{A_\ell}} \quad (39)$$

For dimensional consistency, in Eq. (38) the units of Z vary with the specified values of p , q , and b . For $p = 1$, $q = 1$, and $b = 0$, the units of Z are $\text{kg m}^3/\text{mole}^2 \text{ s}$.

The creation or destruction of gaseous species j by homogeneous gaseous reaction ℓ is calculated from the homogeneous gaseous species yield matrix ($y_{g,j,\ell}$) as:

$$\dot{\omega}_{g,j,\ell}''' = \dot{\omega}_{dA_\ell}''' \max(y_{g,j,\ell}, 0) \quad (40)$$

$$\dot{\omega}_{g,dj,\ell}''' = -\dot{\omega}_{dA_\ell}''' \min(Y_{g,j,\ell}, 0) \quad (41)$$

Note the analogy to Eqs. (24) and (25).

Total species formation rates due to homogeneous gaseous reactions are determined by summing over all reactions (note the analogy to Eqs. (27) and (28)):

$$\dot{\omega}_{g,dj}''' = \sum_{\ell=1}^L \dot{\omega}_{g,dj,\ell}''' \quad (42)$$

$$\dot{\omega}_{g,fj}''' = \sum_{\ell=1}^L \dot{\omega}_{g,fj,\ell}''' \quad (43)$$

The volumetric rate of heat release (or absorption) to the gas phase by homogeneous gaseous reaction ℓ is

$$\dot{Q}_{g,\ell}''' = -\dot{\omega}_{dA_\ell}''' \Delta H_\ell \quad (44)$$

where ΔH_ℓ is the heat of reaction associated with homogeneous gas phase reaction ℓ . Its units are Joules of heat released per unit mass of gas phase species A_ℓ consumed by homogeneous gas phase reaction ℓ . As with condensed phase reactions, positive values of ΔH_ℓ correspond to an endothermic reaction, and negative values correspond to an exothermic reaction.

3.7. Gaseous species total source terms

Gaseous species can be consumed or destroyed in both heterogeneous (solid/gas) and homogeneous (gas/gas) reactions. The source term needed in the gas phase species conservation equation is obtained by summing the contributions from both types of reaction rates:

$$\dot{\omega}_{dj}''' = \dot{\omega}_{s,dj}''' + \dot{\omega}_{g,dj}''' \quad (45)$$

$$\dot{\omega}_{fj}''' = \dot{\omega}_{s,fj}''' + \dot{\omega}_{g,fj}''' \quad (46)$$

All expressions on the RHS have been defined in Eqs. (27), (28), (42), and (43).

4. Governing equations

The one-dimensional control volume system for which the governing equations are derived is shown schematically in Fig. 1. Cell P ("point") has neighboring cells T ("top") and B ("bottom"). The interface between cell P and T is denoted t , and the interface between cell P and B is denoted b . The notation ϕ_T indicates the value of variable ϕ in cell T and ϕ_t indicates the value of variable ϕ at the interface between P and T . $(\delta z)_t$ is the distance from P to T and $(\delta z)_b$ is the distance from P to B . The size (height) of cell P is $(\Delta z)_P$. For calculating source terms, it is assumed that the value of ϕ at the center of a particular cell prevails over the entire cell, but for calculating gradients at cell boundaries it is assumed that ϕ varies in a piecewise linear manner between cell centers. The z dimension increases with depth into the solid, i.e. $z = 0$ corresponds to the surface and $z = \delta$ corresponds to the back face. Note that P is located at the center of each cell, except for the two boundary nodes where P is at the edge (because these are "half" cells). The convention used is that ϕ° denotes the value of ϕ at time t and ϕ denotes the value of ϕ at time $t + \Delta t$.

Gpyro is specifically formulated to accommodate shrinkage and swelling. This is accomplished by assuming that bulk density is a property of a condensed phase species and that each grid cell (having height Δz) is permeable to gaseous mass transfer but is impermeable to condensed phase mass transfer. Thus, if condensed phase bulk density remains constant but gases escape from a cell (e.g., due to pyrolysis) then Δz decreases to conserve

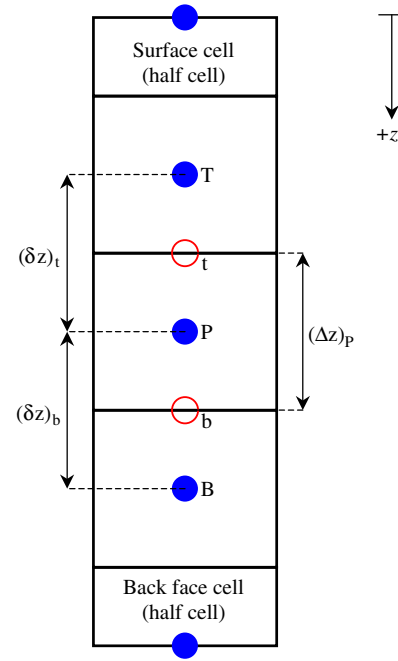


Fig. 1. Control volume system used for discretization.

mass (shrinkage). The same shrinkage occurs if no gases escape but the bulk density increases. Conversely, Δz must increase if the bulk density decreases while no gases escape. A release of gases may occur simultaneously with a change in bulk density; in this case, the change in Δz , if any, is calculated from mass conservation considerations. An increase in porosity (decrease in bulk density) can occur with no change in Δz . Due to this formulation, the grid spacing Δz appears in the conservation equations presented below.

4.1. One-dimensional

4.1.1. Condensed phase mass conservation

The condensed phase mass conservation equation is

$$\frac{(\bar{\rho} \Delta z)_P - (\bar{\rho} \Delta z)_P^\circ}{\Delta t} = -(\dot{\omega}_{fg}''' \Delta z)_P \quad (47)$$

No convective terms are present because, as mentioned above, an assumption of Gpyro is that condensed phase mass does not cross cell boundaries.

4.1.2. Condensed phase species conservation

The condensed phase species conservation equation is similar to the condensed phase mass conservation equation:

$$\frac{(\bar{\rho} Y_i \Delta z)_P - (\bar{\rho} Y_i \Delta z)_P^\circ}{\Delta t} = (\dot{\omega}_{fi}''' \Delta z)_P - (\dot{\omega}_{di}''' \Delta z)_P \quad (48)$$

Here, $\dot{\omega}_{fi}'''$ and $\dot{\omega}_{di}'''$ are, the volumetric total formation and destruction rates of condensed phase species i .

Although it may seem unusual that the grid spacing Δz appears in Eqs. (47) and (48), these conservation equations are well-posed. Eqs. (3), (47), and (48) are $M+2$ equations for $M+2$ unknowns in each grid cell: the M species' mass fractions, $\bar{\rho}$, and Δz .

4.1.3. Gas phase species conservation

In the gas phase species conservation equation, both convective and diffusive transport across cell boundaries must be considered. The convective flux of gaseous species j is $\dot{m}'' Y_j$ and the diffusive flux of gaseous species j is \dot{j}_j'' . The gas phase species

conservation equation is

$$\frac{(\rho_g \bar{\psi} Y_j \Delta z)_p - (\rho_g \bar{\psi} Y_j \Delta z)_p^\circ}{\Delta t} + \dot{m}'' Y_{j|b} - \dot{m}'' Y_{j|t} = -\dot{J}_j''|_b + \dot{J}_j''|_t + (\dot{\omega}_{fj}''' \Delta z)_p - (\dot{\omega}_{dj}''' \Delta z)_p \quad (49)$$

Similar to the condensed phase species conservation equation, $\dot{\omega}_{fj}'''$ is the total formation rate of gaseous species j and $\dot{\omega}_{dj}'''$ is the total destruction rate of gaseous species j . Note that $\dot{\omega}_{fj}'''$ and $\dot{\omega}_{dj}'''$ include contributions from both heterogeneous (gas/solid) and homogeneous (gas/gas) reactions (see Eqs. (45) and (46)).

The diffusive mass flux term in Eq. (49) is calculated assuming Fickian diffusion:

$$\dot{J}_j'' = -\bar{\psi} \rho_g D \frac{\partial Y_j}{\partial z} \quad (50)$$

4.1.4. Condensed phase energy conservation

The condensed phase energy conservation equation is

$$\frac{(\bar{\rho} \bar{h} \Delta z)_p - (\bar{\rho} \bar{h} \Delta z)_p^\circ}{\Delta t} = -\dot{q}''|_b + \dot{q}''|_t - (\dot{Q}_{s-g}''' \Delta z)_p + \left(\sum_{k=1}^K \dot{Q}_{s,k}''' \Delta z \right)_p - \left(\frac{\partial \dot{q}_r''}{\partial z} \Delta z \right)_p + \sum_{i=1}^M ((\dot{\omega}_{fi}''' - \dot{\omega}_{di}''') h_i \Delta z)_p \quad (51)$$

Changes in kinetic energy, potential energy, and work done on the surroundings have been neglected. Fourier's law is used to calculate \dot{q}'' , the conductive heat flux through the condensed phase:

$$\dot{q}'' = -\bar{k} \frac{\partial T}{\partial z} \quad (52)$$

$\dot{Q}_{s,k}'''$ is the volumetric rate of heat release or absorption due to condensed phase reactions, defined in Eq. (36). \dot{Q}_{s-g}''' is the volumetric rate of heat transfer from the condensed phase to the gas phase. Although \dot{Q}_{s-g}''' is sometimes neglected altogether in pyrolysis models on the basis that it is small, Gpyro provides two different options for calculating \dot{Q}_{s-g}''' . In the first, used in this paper, thermal equilibrium between the gas phase and the condensed phase is assumed. This is called the thermal equilibrium formulation. In the second, called two-temperature formulation, the gas phase temperature is different from the condensed phase temperature and the rate of heat transfer from the solid to the gas is explicitly calculated (see the Gpyro technical reference [13] for details). Under the thermal equilibrium approximation used in this paper, \dot{Q}_{s-g}''' is calculated as

$$\dot{Q}_{s-g}''' = -\dot{Q}_{g-s}''' = \dot{m}'' c_{pg} \frac{\partial T}{\partial z} - \sum_{\ell=1}^L \dot{Q}_{g,\ell}''' \quad (53)$$

As described in the Gpyro technical reference [13], Eq. (53) assumes that $\rho_g \bar{\psi} c_{pg} \ll \bar{\rho} \bar{c}$ and $\bar{\psi} k_g \ll \bar{k}$. Note that $\sum_{\ell=1}^L \dot{Q}_{g,\ell}'''$ is the volumetric rate of heat release due to homogeneous gaseous reactions. Essentially, with the thermal equilibrium approach, any heat released by gas phase reactions is added directly to the solid instead of the gas (as in the two-temperature/thermal non-equilibrium formulation).

The divergence of the in-depth radiative heat flux vector in Eq. (51) is calculated as

$$\frac{\partial \dot{q}_r''}{\partial z} = -\bar{\epsilon} \dot{q}_e'' \bar{\kappa}(z) \exp\left(-\int_0^z \bar{\kappa}(\zeta) d\zeta\right) \quad (54)$$

Eq. (54) assumes that radiation is applied only normal to the exposed surface and interior radiative emission is negligible, i.e. penetration of radiation into the solid is calculated, but the emission from interior parts of the solid is not.

A decomposing solid frequently consists of a single “layer”. However, Gpyro can accommodate materials with a layered or laminated composition. For layers that are not in perfect thermal contact, the rate of heat transfer between layers calculated as $h_{cr} \Delta T$, where h_{cr} is an inverse contact resistance (contact conductance) with units of W/m²K and ΔT is the temperature difference between the “back” of one layer and the “front” of the layer that it abuts. At the interface between two layers that are not in perfect thermal contact, the thermal conductivity \bar{k} in Eq. (52) is replaced with $h_{cr} \times \delta z$, where δz is the appropriate distance between cell centers.

4.1.5. Gas phase energy conservation

Under thermal equilibrium, the gas phase energy conservation equation is

$$T_g = T \quad (55)$$

As mentioned earlier, Gpyro natively supports a two-temperature or thermal non-equilibrium formulation (see the Gpyro technical reference guide [13] for details). However, the simulations presented in this paper assume that thermal equilibrium exists between the gaseous and the condensed phases so Eq. (55) is applied.

4.1.6. Pressure evolution equation

An equation describing the evolution of the pressure profile inside the decomposing solid is obtained from the gas phase mass conservation equation:

$$\frac{(\rho_g \bar{\psi} \Delta z)_p - (\rho_g \bar{\psi} \Delta z)_p^\circ}{\Delta t} + \dot{m}''|_b - \dot{m}''|_t = (\dot{\omega}_{fg}''' \Delta z)_p \quad (56)$$

Note that the source term is equal in magnitude to, but has the opposite sign of, the source term that appears in the condensed phase mass conservation equation. Darcian flow is assumed:

$$\dot{m}''|_b = -\left(\frac{\bar{K}}{v}\right)_b \frac{\partial P}{\partial z}|_b \quad (57a)$$

$$\dot{m}''|_t = -\left(\frac{\bar{K}}{v}\right)_t \frac{\partial P}{\partial z}|_t \quad (57b)$$

For simplicity, Eq. (57) (used in this paper) does not include a buoyancy contribution, but the Gpyro technical reference describes the more general case where buoyancy is included. A pressure evolution equation is obtained from Eq. (56) by replacing ρ_g with P using the ideal gas law and substituting Eq. (57):

$$\begin{aligned} & \frac{\left(\frac{P \bar{M}}{RT_g} \bar{\psi} \Delta z\right)_p - \left(\frac{P \bar{M}}{RT_g} \bar{\psi} \Delta z\right)_p^\circ}{\Delta t} \\ & = \left(\frac{\bar{K}}{v}\right)_b \frac{\partial P}{\partial z}|_b - \left(\frac{\bar{K}}{v}\right)_t \frac{\partial P}{\partial z}|_t + (\dot{\omega}_{fg}''' \Delta z)_p \end{aligned} \quad (58)$$

Eq. (58) can be solved for P because all other quantities are calculated elsewhere.

4.2. Zero-dimensional

Gpyro can solve 0D transient equations that represent the mass and species evolution of a homogeneous particle having negligible gradients of temperature species as occurs in idealized thermal analysis experiments (thermogravimetric analysis and differential scanning calorimetry). Zero-dimensional transient forms of the governing equations are presented below.

Condensed phase mass conservation:

$$\frac{(\bar{\rho} \Delta z) - (\bar{\rho} \Delta z)^\circ}{\Delta t} = -\dot{\omega}_{fg}''' \Delta z \quad (59)$$

Condensed phase species conservation:

$$\frac{(\bar{\rho}Y_i \Delta z) - (\bar{\rho}Y_i \Delta z)^\circ}{\Delta t} = \dot{\omega}_{fi}''' \Delta z - \dot{\omega}_{di}''' \Delta z \quad (60)$$

Gas phase mass conservation:

$$\frac{(\rho_g \bar{\psi} \Delta z) - (\rho_g \bar{\psi} \Delta z)^\circ}{\Delta t} = \dot{\omega}_{fg}''' \Delta z \quad (61)$$

Gas phase species conservation:

$$Y_j = Y_j^\infty \quad (62)$$

Condensed phase energy conservation:

$$T = T_0 + \beta t \quad (63)$$

Gas phase energy conservation:

$$T_g = T = T_0 + \beta t \quad (64)$$

Gas phase momentum conservation:

$$P = P_\infty \quad (65)$$

Here, β is the linear ramp rate in K/s. The temperature and gas phase mass fractions are taken as the ambient values. Thus, for the 0D transient formulation, T and Y_j are specified by the user rather than calculated.

Differential thermogravimetric (DTG) curves ($d/dt(m/m_0)$) and thermogravimetric curves (m/m_0) can be calculated from the

Table 4

Gaseous yields for PMMA simulations (only nonzero yields shown).

| <i>j</i> | <i>k</i> | | |
|--------------------------|----------|------|-------|
| | 1 | 2 | 3 |
| 1 (thermal pyrolysate) | | 1.00 | |
| 2 (oxygen) | | | −0.05 |
| 3 (nitrogen) | | | |
| 4 (oxidative pyrolysate) | | | 1.05 |

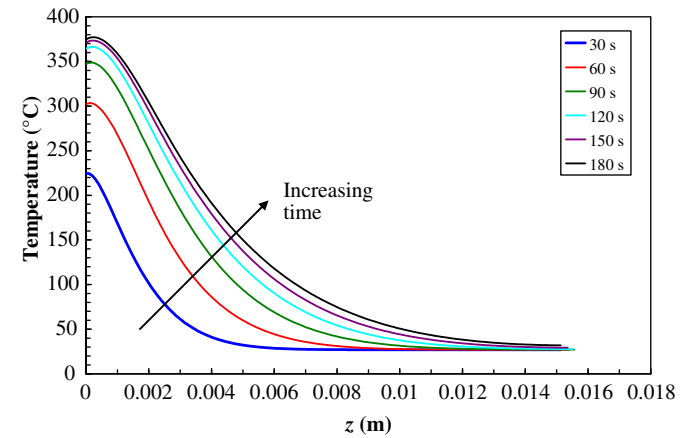


Fig. 2. Calculated temperature profile for PMMA irradiated at 40 kW/m² under 40% O₂.

Table 1

Boundary condition parameters for simulations of thermal irradiation of PMMA, white pine, and intumescent coating.

| | \dot{q}_e'' (kW/m²) | Y_j^∞ Oxygen (–) | Y_j^∞ Nitrogen (–) | T_∞ (K) | P_∞ (kPa) | h_c (W/m² K) | $h_{c\delta}$ (W/m² K) |
|-------------|-----------------------|----------------------------|------------------------------|----------------|------------------|-------------------|------------------------|
| PMMA | 40 | 0.000 | 1.000 | 300 | 101.3 | 10.0 | 10.0 |
| | 40 | 0.113 | 0.887 | 300 | 101.3 | 10.0 | 10.0 |
| | 40 | 0.222 | 0.778 | 300 | 101.3 | 10.0 | 10.0 |
| | 40 | 0.432 | 0.568 | 300 | 101.3 | 10.0 | 10.0 |
| | 17 | 0.000 | 1.000 | 300 | 101.3 | 10.0 | 10.0 |
| | 17 | 0.113 | 0.887 | 300 | 101.3 | 10.0 | 10.0 |
| | 17 | 0.222 | 0.778 | 300 | 101.3 | 10.0 | 10.0 |
| | 17 | 0.432 | 0.568 | 300 | 101.3 | 10.0 | 10.0 |
| Pine | 40 | 0.000 | 1.000 | 300 | 101.3 | 10.0 ^a | 10.0 |
| | 25 | 0.000 | 1.000 | 300 | 101.3 | 10.0 ^a | 10.0 |
| Intumescent | 90 | 0.000 | 1.000 | 300 | 101.3 | 10.0 | 2.0 |

(–) denotes dimensionless.

^a $h_{c,nb}$.

Table 2

Condensed phase parameters for PMMA simulations.

| <i>i</i> | Name | k_0 (W/m K) | n_k (–) | ρ_0 (kg/m³) | n_ρ (–) | c_0 (J/kg K) | n_c (–) | ε (–) | κ (m⁻¹) | γ (m) | K (m²) | ρ_{s0} (kg/m³) |
|----------|-------|---------------|-----------|------------------|--------------|----------------|-----------|-------------------|----------------|--------------|---------------------|---------------------|
| 1 | pmma | 0.20 | −0.19 | 1190 | −0.12 | 1606 | 0.89 | 0.86 | 1980 | 0 | 1×10^{-10} | 1200 |
| 2 | bpmma | 0.18 | −0.18 | 1036 | −0.14 | 1667 | 0.72 | 0.87 | 1000 | 0 | 1×10^{-10} | 1200 |

(–) denotes dimensionless.

Table 3

Reaction parameters for PMMA simulations.

| <i>k</i> | From | To | χ (–) | ΔH_{sol} (J/kg) | ΔH_{vol} (J/kg) | Z (s⁻¹) | E (kJ/mol) | n (–) | n_{O_2} (–) |
|----------|-------|-------|------------|-------------------------|-------------------------|-----------------------|--------------|---------|---------------|
| 1 | pmma | bpmma | 0 | 0 | 0 | 2.31×10^{10} | 115.3 | 1.04 | 0 |
| 2 | bpmma | Gases | 1 | 0 | 7.28×10^5 | 4.89×10^{13} | 197.6 | 1.16 | 0 |
| 3 | bpmma | Gases | 1 | 0 | 4.53×10^5 | 9.47×10^{13} | 186.3 | 1.30 | 1.31 |

(–) denotes dimensionless.

above relations. A DTG curve is calculated as

$$\frac{d}{dt} \left(\frac{m''}{m_0''} \right) = - \frac{\dot{\omega}_{fg}'' \Delta z}{m_0''} = - \frac{\dot{\omega}_{fg}'' \Delta z}{(\rho \Delta z)|_{t=0}} \quad (66)$$

Integrating the DTG curve gives the TG curve:

$$\frac{m''}{m_0''}(t) = 1 - \frac{1}{m_0''} \int_0^t \dot{\omega}_{fg}''(\tau) \Delta z(\tau) d\tau \quad (67)$$

5. Numerical solution methodology

The governing equations presented above yield a system of coupled algebraic equations that are solved numerically. The

recommendations of Patankar [18] are followed. Due to non-linearity introduced by the source terms and temperature-dependent thermophysical properties, a fully implicit formulation is adopted. Gas phase species, gas phase momentum, and condensed phase energy conservation equations are solved using a computationally efficient tridiagonal matrix algorithm. The condensed phase mass and condensed phase species conservation equations are solved with a fully implicit solver that uses relaxation to prevent divergence. Source terms are split into positive and negative components to ensure prevent negative mass fractions or densities from occurring [18]. Newton iteration is used to extract the temperature from the weighted enthalpy and the condensed phase species mass fractions. Details are given in the Gpyro technical reference [13].

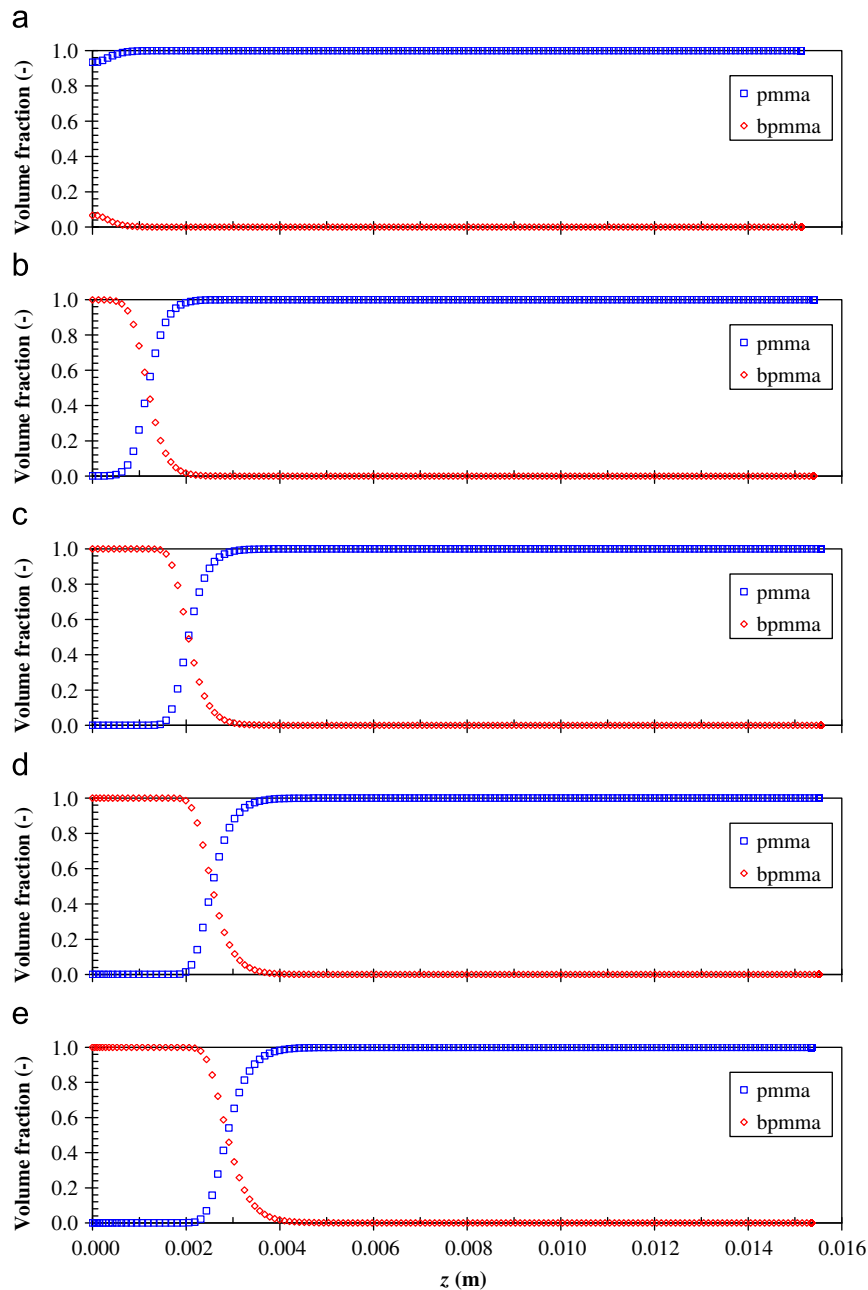


Fig. 3. Calculated volume fraction of condensed phase species pmma and bpmma (bubbled pmma) for PMMA irradiated at 40 kW/m² under 40% O₂. (a) 30 s; (b) 60 s; (c) 90 s; (d) 120 s; (e) 150 s.

Boundary conditions in Gpyro are general [13]. However, the boundary conditions described in Section 6 describe the experimental configurations being simulated.

6. Sample calculations

In this section, Gpyro is used to simulate four specific experiments. The first three simulations (Section 6.1) involve pyrolysis in the cone calorimeter (or similar apparatuses). They are: (1) thermo-oxidative decomposition of a noncharring thermoplastic, PMMA (Section 6.1.1); (2) anaerobic pyrolysis of a charring material, white pine (Section 6.1.2); and (3) gasification and swelling of an intumescent coating (Section 6.1.3). Finally, smolder wave propagation in polyurethane foam is simulated in Section 6.2.

In all simulations, the initial grid spacing is 0.1 mm, except for the intumescent coating simulation (Section 6.1.3) where 0.02 mm is used. The timestep is constant at 0.1 s. Gaseous specific heat capacity is 1100 J/kg K. Chapman–Enskog parameters are taken from Bird et al. [17], and generic gaseous surrogate species (such as “pyrolysate”) that have unknown molecular composition are assumed to have properties of propane. In all heterogeneous reactions, $T_{crit,k} = 0$ K.

6.1. Cone calorimeter (and similar) experiments

The first three experiments simulated here involve irradiating solid combustibles at one face, as in a typical cone calorimeter experiment. Initial conditions (species mass fractions, temperature, and pressure) and boundary conditions are specified to represent the experimental configuration as closely as possible. The boundary conditions that describe these experiments are discussed below.

The gas phase species conservation equation (Eq. (49)) requires boundary conditions for each gaseous species at $z = 0$ and δ . The back face ($z = \delta$) is assumed impermeable, so there is no mass flux of volatiles across the back face:

$$\left. \frac{\partial Y_j}{\partial z} \right|_{z=\delta} = 0 \quad (68a)$$

The diffusive mass flux of gaseous species at $z = 0$ is approximated as

$$-\tilde{\rho} \tilde{D}_g \left. \frac{\partial Y_j}{\partial z} \right|_{z=0} \approx \frac{h_c}{c_{pg}} (Y_j^\infty - Y_j|_{z=0}) \quad (68b)$$

In Section 6.1.2 only, the effect of blowing on the heat transfer coefficient is simulated using a Couette flow approximation [19]:

$$h_c = \frac{\dot{m}_0'' c_{pg}}{\exp(\dot{m}_0'' c_{pg} / h_{c,nb}) - 1} \quad (69)$$

where $h_{c,nb}$ is the heat transfer coefficient with no blowing, and \dot{m}_0'' is the mass flux of gases at $z = 0$.

The condensed phase energy conservation equation (Eq. (51)) requires two boundary conditions. The front face boundary condition is

$$-\tilde{k} \left. \frac{\partial T}{\partial z} \right|_{z=0} = \tilde{\epsilon} \dot{q}_e'' - h_c (T|_{z=0} - T_\infty) - \tilde{\epsilon} \sigma (T^4|_{z=0} - T_\infty^4) \quad (\text{for } \tilde{k}|_{z=0} \rightarrow \infty) \quad (70a)$$

$$-\tilde{k} \left. \frac{\partial T}{\partial z} \right|_{z=0} = -h_c (T|_{z=0} - T_\infty) - \tilde{\epsilon} \sigma (T^4|_{z=0} - T_\infty^4) \quad (\text{for } \tilde{k}|_{z=0} \neq \infty) \quad (70b)$$

The back face boundary condition is

$$-\tilde{k} \left. \frac{\partial T}{\partial z} \right|_{z=\delta} = h_{c\delta} (T|_{z=\delta} - T_\infty) \quad (70c)$$

The pressure evolution equation (Eq. (58)) requires two boundary conditions. The boundary condition at the front face sets the pressure equal to the atmospheric value:

$$P|_{z=0} = P_\infty \quad (71a)$$

The pressure gradient at the back face is set to zero to give an impermeable back face:

$$\left. \frac{\partial P}{\partial z} \right|_{z=\delta} = 0 \quad (71b)$$

Boundary condition parameters for each simulation are summarized in Table 1.

6.1.1. Noncharring gasification—PMMA

Thermal decomposition of PMMA has been extensively investigated. The senior author's research group has published several studies on PMMA ignition and flammability, including transient mass loss rate curves prior to ignition. However, long-duration transient mass loss rate data are necessary to estimate heats of reaction that control quasi-steady burning.

By measuring long-duration transient mass loss rates of PMMA slabs irradiated under nonflaming conditions at 17 and 40 kW/m² in atmospheres ranging from nitrogen to 40% oxygen/60%

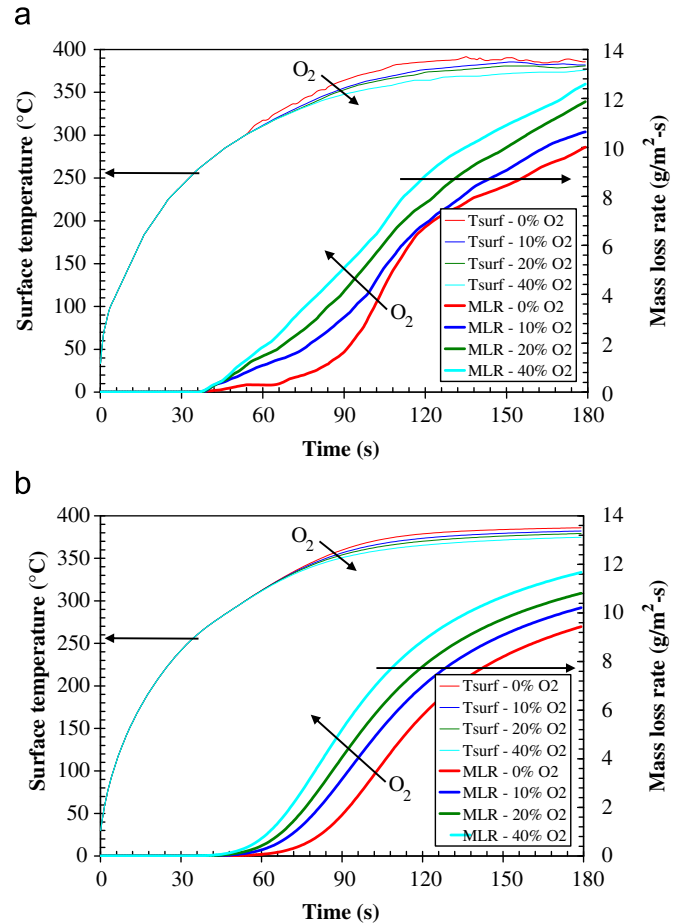
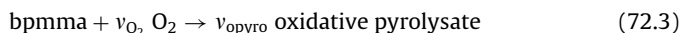


Fig. 4. Surface temperature and mass loss rate of PMMA irradiated at 40 kW/m². (a) Experimental data [20]; (b) Optimized model calculations.

nitrogen (by volume), Kashiwagi and Ohlemiller [20] showed that bulk decomposition of PMMA is sensitive to oxygen concentration. It was found that mass loss rate increases with oxygen content of the atmosphere, but surface temperature decreases due to the endothermicity of the pyrolysis reaction. Oxygen sensitivity is more noticeable at 17 kW/m² irradiance than 40 kW/m². Due to these interesting phenomena, this set of experiments is well-suited to test Gpyro's predictive capabilities.

Two condensed phase species are considered in the simulations: pmma and bpmma. The latter is “bubbled” PMMA, which has a nonzero porosity and allows gases to diffuse from the ambient into the bubble layer. Oxidative reaction rates are related to the local oxygen concentration inside the decomposing solid, rather than the freestream value. In-depth radiation absorption is modeled by using a finite absorption coefficient. The experiments were conducted under natural convection, and a convective heat transfer coefficient of 10 W/m² K is assumed for the simulations.

Four gaseous species are tracked: thermal pyrolysate, oxygen, nitrogen, and oxidative pyrolysate. The assumed three-step reaction mechanism is given by



Tables 2–4 list the model input parameters that were estimated using genetic algorithm optimization from the experiments [20] at both irradiance levels.

Fig. 2 shows the temperature profiles calculated with the optimized model for a heat flux of 40 kW/m² and an oxygen mole fraction of 0.40. At later times, the diathermancy of the bubble layer becomes apparent as the temperature peak occurs slightly in-depth rather than immediately at the irradiated surface. Fig. 3 shows the calculated microstructure (composition of the condensed phase) at several different times. Around 30 s, the surface temperature is approximately 250 °C, and species bpmma (bubbled pmma) starts to form as can be seen from Fig. 3a. By 150 s (Fig. 3e), the bubble layer has penetrated more than 3 mm toward the interior of the solid.

The 40 kW/m² experimental data and model calculations using the optimized model input parameters are shown separately at all oxygen concentrations in Fig. 4. Qualitatively, the curves appear similar, and Gpyro correctly reproduces the experimentally observed trend of decreasing surface temperature with increasing ambient oxygen concentration. Comparisons of model calculations and experimental data at individual oxygen concentrations are shown in Fig. 5. It can be seen that there is good agreement between model calculations and experimental data.

The 17 kW/m² experimental data at all oxygen levels are shown in Fig. 6a, and Gpyro calculations are shown in Fig. 6b. The curves appear qualitatively similar, but it is evident that there are some quantitative differences. Detailed comparisons between

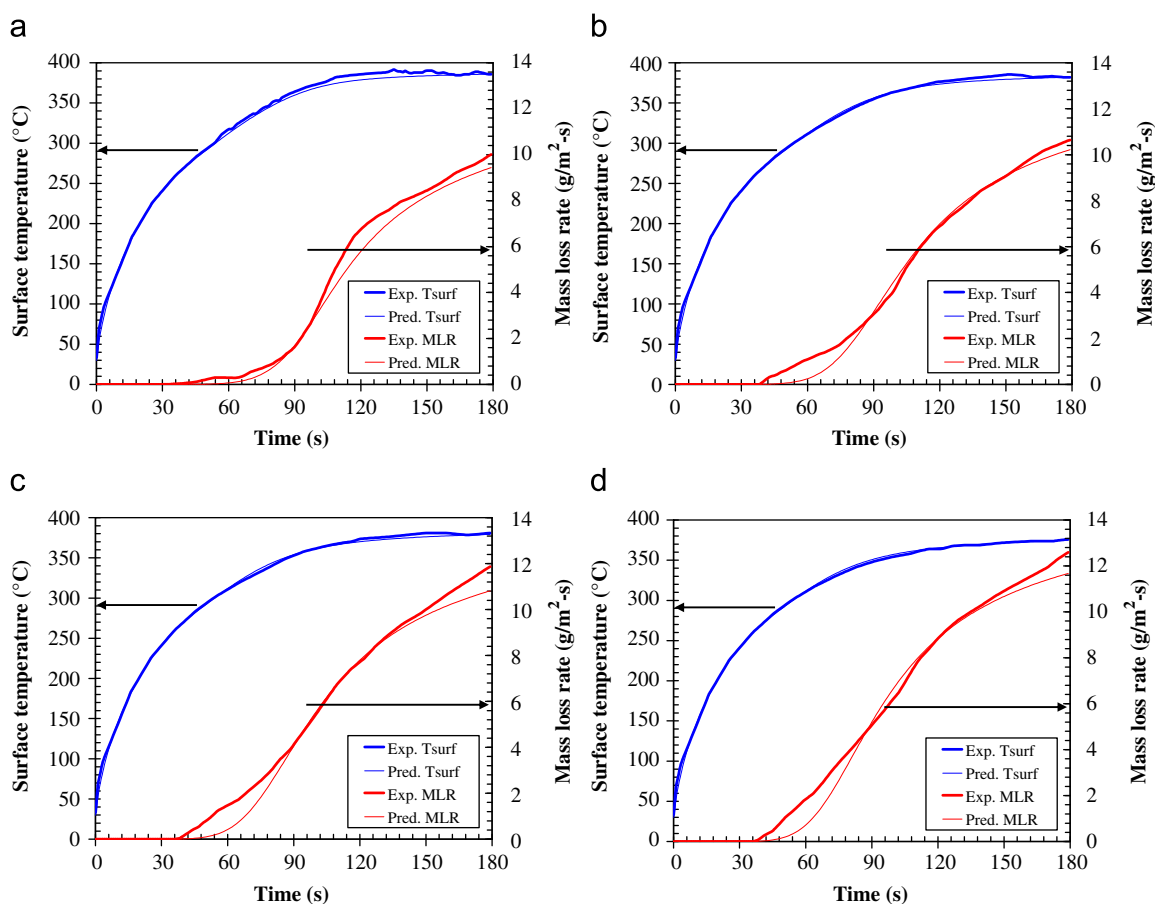


Fig. 5. Comparison of experimental [20] and modeled surface temperature and mass loss rates of PMMA irradiated at 40 kW/m². (a) Nitrogen atmosphere; (b) 10% O₂ atmosphere; (c) 20% O₂ atmosphere; (d) 40% O₂ atmosphere.

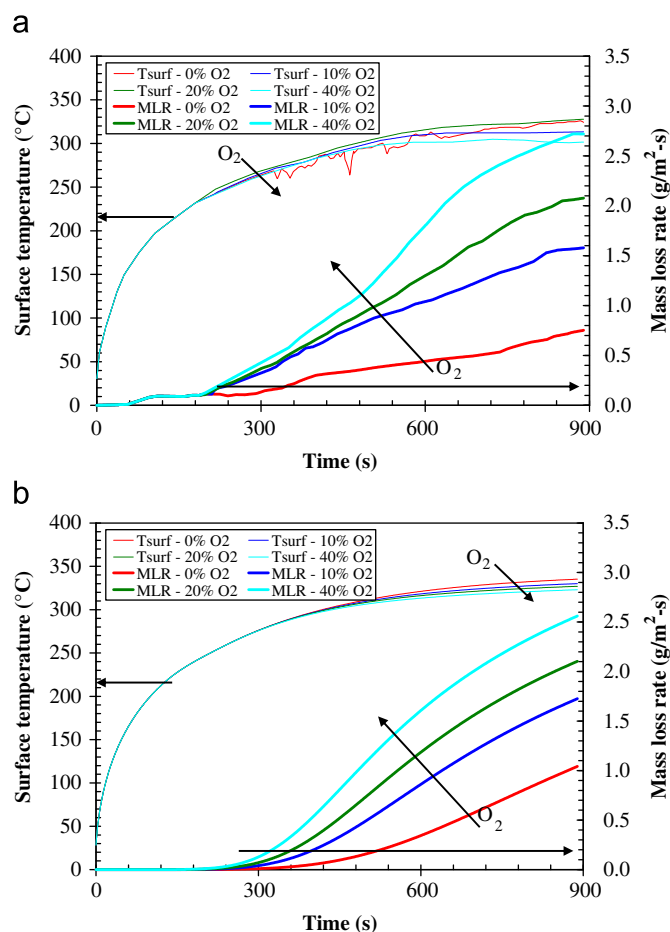


Fig. 6. Surface temperature and mass loss rate of PMMA irradiated at 17 kW/m^2 . (a) Experimental data [20]; (b) Model.

model calculations and experimental data are shown in Figs. 7a–d. It can be seen that the model correctly captures the experimentally observed increase in the oxygen sensitivity at 17 kW/m^2 irradiance compared with 40 kW/m^2 . Although the model over predicts the surface temperature by as much as 15°C , the mass loss rate is well predicted.

Since the experiments used to extract the material properties do not include a quasi-steady period where mass loss rates approach an approximately constant value, steady-state mass loss rates were calculated (for non-oxidative conditions) as a function of total applied heat flux and compared to experimental data for steady burning compiled by Kwon et al. [21] for black PMMA (2.5 cm thickness). These experimental data were not used as part of the material property estimation process. Fig. 8 compares the measured and modeled quasi-steady mass loss rates. The x-axis in Fig. 8 is the total applied heat flux (external radiation plus flame heat transfer) assuming flame heat flux of 20 kW/m^2 . It can be seen that calculated quasi-steady mass loss rates agree well with steady burning experimental data up to a total applied heat flux of 100 kW/m^2 .

The model input parameters determined by genetic algorithm optimization, listed in Tables 2–4, are consistent with literature data. The thermal conductivity and specific heat capacity extracted by genetic algorithm optimization are compared with literature values [22] in Fig. 9 (model values were extracted from the 40 kW/m^2 , 40% O_2 simulations at 180 s). Optimized in-depth absorption coefficients (1980 m^{-1} for pmma and 1000 m^{-1} for

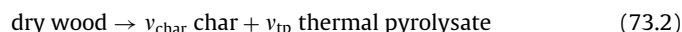
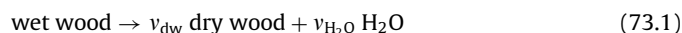
bpmma) are consistent with those reported by Manohar et al. [23] for PMMA ($170\text{--}3895 \text{ m}^{-1}$ depending on wavelength). The optimized surface emissivity (0.86 for pmma and 0.87 for bpmma) is close to the value of 0.85 reported by Hallman et al. [24] for clear PMMA irradiated by a blackbody at 1000 K. The optimized heats of volatilization (728 kJ/kg for thermal pyrolysis and 453 kJ/kg for oxidative pyrolysis) are similar to literature values (687 kJ/kg [25] to 1080 kJ/kg [26] under nitrogen and 550 kJ/kg under air [26]).

6.1.2. Charring gasification—white pine

Ohlemiller et al. [27,28] experimentally studied the effects of ambient oxygen concentration on the nonflaming gasification of irradiated white pine. Ref. [28] contains mass loss rate measurements at multiple heat flux levels and oxygen concentrations as well as surface and in-depth thermocouple temperature measurements. In the experiments, white pine cubes 3.8 cm on edge were irradiated at 25 and 40 kW/m^2 in oxygen concentrations of 0% (nitrogen), 10.5%, and 21% by volume. The initial pine density was approximately 380 kg/m^3 , with an initial moisture content of approximately 5% by mass.

These experiments [28] have been simulated by Jia et al. [29] and Weng et al. [30] using integral charring models. Jia et al. [29] modeled only the experiments [28] that were conducted under nitrogen because their model did not include exothermic char oxidation. Both the nitrogen and oxidative experiments have been simulated with Gpyro, but only the nitrogen modeling is presented here because the oxidative simulations are the subject of a separate publication [31].

The simulations consider three condensed phase species: (1) wet wood, (2) dry wood, and (3) char. The gas phase is comprised of three species: (1) thermal pyrolysate, (2) nitrogen, and (3) water vapor. A two-step reaction mechanism is implemented:



Thermal properties of all condensed phase species vary with temperature. Radiative heat transfer across char pores is modeled, and condensed phase species have different emissivities to account for blackening of the surface as charring occurs. Model input parameters (given in Tables 5–7) are estimated by genetic algorithm optimization from experimental data at both heat flux levels.

The calculated pine microstructure is shown in Fig. 10 at several different times. It can be seen that by 100 s (Fig. 10a), char has started to form near the irradiated surface ($z = 0$) and the moisture evaporation front has propagated approximately 4 mm from the surface. At later times, the moisture evaporation front propagates deeper into the solid, although at a decreasing rate due to the insulating effect of the char forming near the surface.

A comparison of Gpyro calculations using the optimized model parameters and the experimental temperature data for the 40 kW/m^2 experiment is shown in Fig. 11. The surface temperature is slightly over-predicted, but the calculated temperatures at 5 and 10 mm match the experimental data very well. The mass loss rate is also well predicted, except that the peak mass loss rate is under-predicted by $<10\%$ and occurs $\sim 10 \text{ s}$ earlier than in the experiment.

A comparison of model calculations and experimental data is given in Fig. 12 for the 25 kW/m^2 experiment. It can be seen that the shapes of the curves match well, but the peak mass loss rate is over-predicted by $\sim 25\%$ and the peak occurs approximately 2 min earlier in the model than in the experiment.

Discrepancies between Gpyro calculations and experimental data may be attributed to the simplified reaction mechanism and

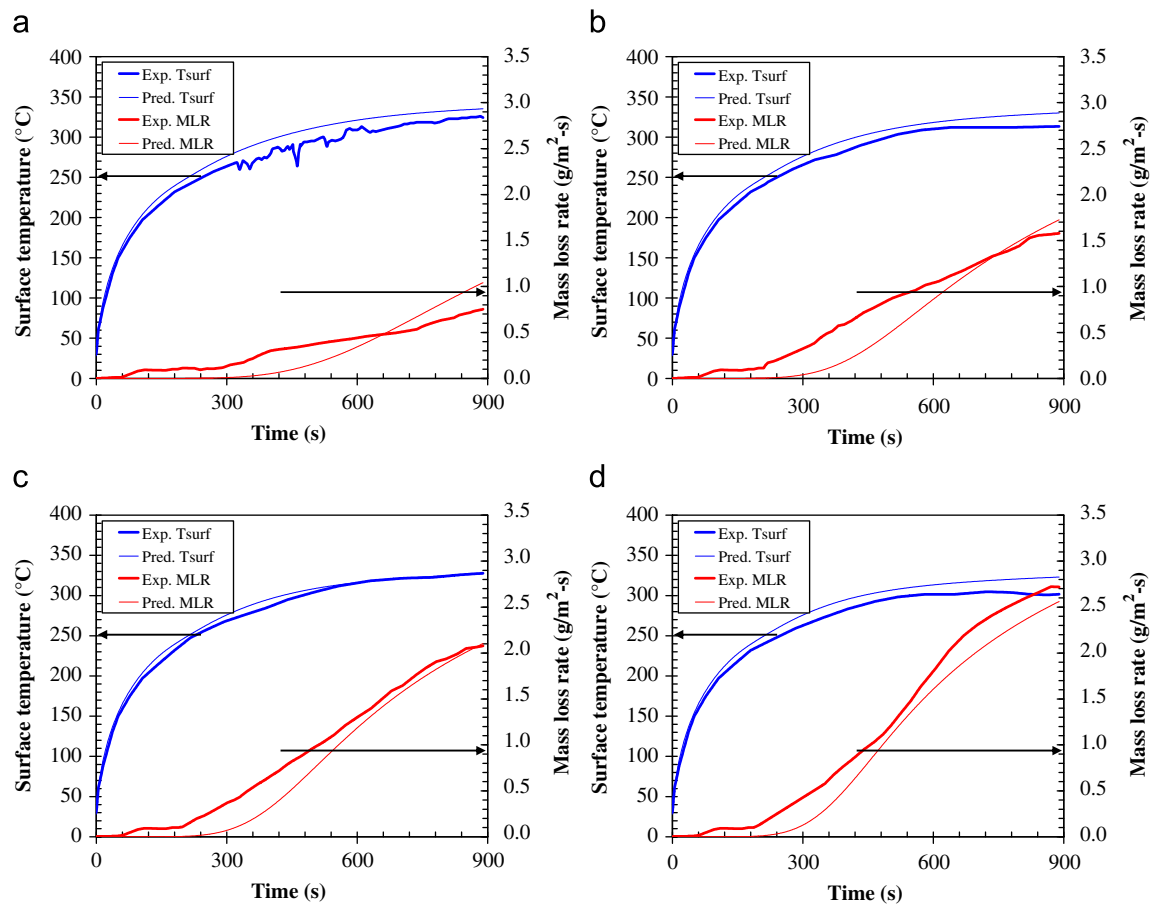


Fig. 7. Comparison of experimental [20] and modeled surface temperature and mass loss rates of PMMA irradiated at 17 kW/m². (a) Nitrogen atmosphere; (b) 10% O₂ atmosphere; (c) 20% O₂ atmosphere; (d) 40% O₂ atmosphere.

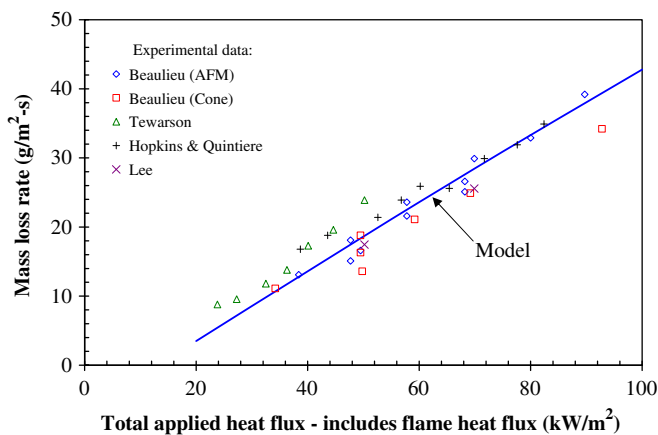


Fig. 8. Comparison of modeled and measured quasi-steady mass loss rates for PMMA combustion. Experimental data compiled by Kwon et al. [21].

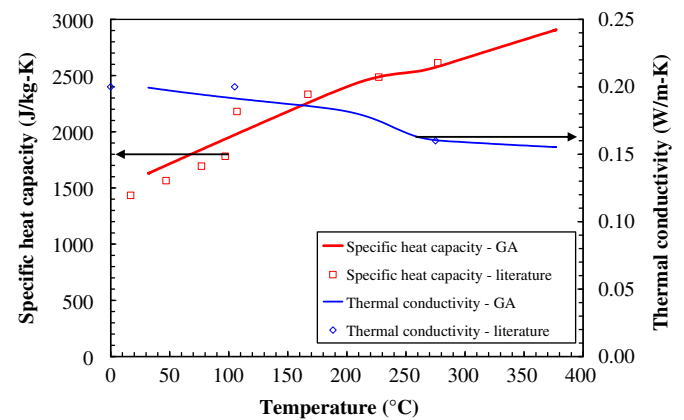


Fig. 9. Comparison of PMMA thermal conductivity and specific heat capacity determined by genetic algorithm optimization and literature data [22].

decomposition kinetics used here. At lower heat flux levels, temperatures are lower and decomposition kinetics play a more significant role than at higher heat flux levels where mass loss rates are controlled primarily by a heat balance. Thus, slight inaccuracies in the decomposition kinetics may lead to larger discrepancies between the model calculations and experimental data at lower heat flux levels.

6.1.3. Intumescent coating

An intumescent material or coating swells when heated to form a porous low-density char, thereby reducing the heat transfer to the underlying virgin material. Intumescent coatings are sometimes applied to steel structural members to achieve the fire resistance ratings required by building codes. Modeling the process of intumescence is considerably more complicated than

Table 5

Condensed phase parameters for white pine simulations.

| <i>i</i> | Name | k_0 (W/m K) | n_k (–) | ρ_0 (kg/m ³) | n_p (–) | c_0 (J/kg K) | n_c (–) | ε (–) | κ (m ^{–1}) | γ (m) | K (m ²) | ρ_{s0} (kg/m ³) |
|----------|----------|---------------|-----------|-------------------------------|-----------|----------------|-----------|-------------------|-----------------------------|----------------------|-----------------------|----------------------------------|
| 1 | wet wood | 0.186 | 0.185 | 380 | 0 | 1764 | 0.406 | 0.757 | ∞ | 0 | 1×10^{-10} | 390 |
| 2 | dry wood | 0.176 | 0.594 | 360 | 0 | 1664 | 0.660 | 0.759 | ∞ | 0 | 1×10^{-10} | 390 |
| 3 | char | 0.065 | 0.435 | 73.0 | 0 | 1219 | 0.283 | 0.957 | ∞ | 3.3×10^{-3} | 1×10^{-10} | 390 |

(–) denotes dimensionless.

Table 6

Reaction parameters for white pine simulations.

| <i>k</i> | From | To | χ (–) | ΔH_{sol} (J/kg) | ΔH_{vol} (J/kg) | Z (s ^{–1}) | E (kJ/mol) | n (–) | n_{O_2} (–) |
|----------|----------|----------|------------|-------------------------|-------------------------|------------------------|--------------|---------|---------------|
| 1 | wet wood | dry wood | 1 | 0 | 2.41×10^6 | 4.29×10^3 | 43.8 | 0.99 | 0 |
| 2 | dry wood | char | 1 | 0 | 5.33×10^5 | 3.29×10^9 | 135.0 | 4.78 | 0 |

(–) denotes dimensionless.

Table 7

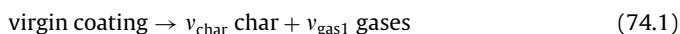
Gaseous yields for white pine simulations (only nonzero yields shown).

| <i>j</i> | <i>k</i> |
|------------------------|----------|
| | 1 |
| 1 (thermal pyrolysate) | 1 |
| 2 (nitrogen) | |
| 3 (water vapor) | 1 |

modeling thermoplastic or charring materials due to large changes in density and volume.

Griffin et al. [32] experimentally studied the effect of atmospheric oxygen concentration on intumescent coatings using thermogravimetry, differential thermal analysis, and cone calorimetry. In this section, Gpyro is used to simulate their “material A”, an epoxy-based intumescent coating with inorganic filler consisting of glass/silica fibers. The experiments simulated include thermogravimetric tests conducted under nitrogen (heating rates of 10, 15, 20, and 30 °C/min) and cone calorimeter tests conducted at an irradiance of 90 kW/m² in a “reduced O₂” atmosphere having an oxygen concentration between 8% and 10%. The intumescent coating tested in the cone calorimeter was applied manually onto a mild steel plate having a thickness of 3 mm. The assembly was then mounted in specially designed calcium silicate sample holder that permits optical measurement of the coating thickness as it swells.

In this set of simulations, the effect of oxygen on the decomposition reactions is not explicitly modeled. Four condensed phase species are considered: virgin coating, char, ash, and steel. Two reactions are considered (Eq. (74)). The first converts species “virgin coating” to char and gases and causes intumescence. The second reaction converts char to ash and gases:



In the simulations, the intumescent coating/steel plate system is modeled as two distinct layers. The top layer is the intumescent coating. It has a thickness of 2.7 mm and the initial mass fraction of condensed phase species virgin coating is specified as 1.0 in this layer. The second layer is the steel plate, having a thickness of 3 mm. The initial mass fraction of condensed phase species steel is

specified as 1.0 in this layer. The assumed inverse contact resistance (contact conductance) between the intumescent coating and the steel plate is 100 W/m² K. In-depth absorption of radiation is not modeled ($\kappa \rightarrow \infty$), but radiation heat transfer across pores is considered. The density of the intumescent coating is not indicated in Ref. [32], so it is estimated to be 1000 kg/m³.

As with the other simulations, genetic algorithm optimization is used to estimate the model input parameters. The optimization process is conducted in two stages. First, kinetic parameters are estimated from the thermogravimetric data. Then, reaction kinetics are held fixed and the thermal properties and reaction enthalpies are estimated from the cone calorimeter data. The resultant set of model parameters is presented in Tables 8 and 9.

A comparison of the experimental differential thermogravimetric curves and those calculated with Gpyro is shown in Fig. 13. The main features of the experimental curves are captured, but all of the details are not. However, this is to be expected since only two reactions are considered.

Next, the remaining model input parameters are determined from the cone calorimeter experiments while holding constant the kinetics parameters extracted from the thermogravimetric experiments. Fig. 14 shows the temperature profiles calculated with the optimized model at several different times. Note that the intumescent coating increases in thickness by a factor of almost 20.

Fig. 15 compares the modeled and experimentally measured substrate temperature and coating thickness. The substrate temperature is well predicted, differing from the experimental data by no more than 50 °C over the 30 min experiment. There is also good agreement between the measured and calculated transient thickness of the coating as it increases in thickness.

6.2. Smolder—polyurethane foam

The final Gpyro simulation presented here is forward propagation of a smolder wave in polyurethane foam [33]. The experimental configuration involves smolder in a polyurethane foam cylinder 12 cm in diameter and 14 cm in length. The experiments were conducted in microgravity on the NASA Space Shuttle (missions STS-105 and STS-108). Temperatures were measured with centerline thermocouples installed at eight axial locations. The smolder reaction was initiated with a porous igniter at one end of the cylinder ($z = 14$ cm). Air was forced into the foam sample at the igniter end so that the smolder wave propagated in

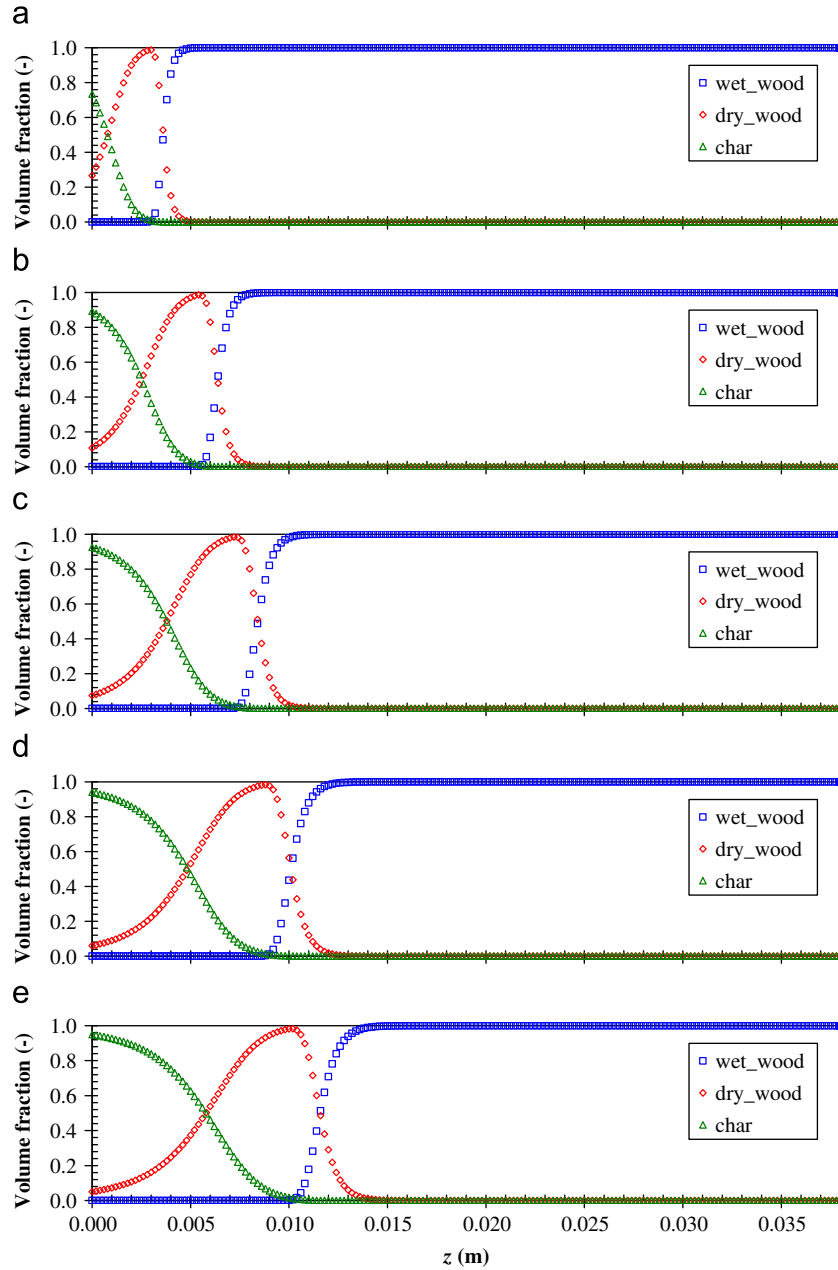


Fig. 10. White pine microstructure (condensed phase volume fractions). (a) 100 s; (b) 200 s; (c) 300 s; (d) 400 s; (e) 500 s.

the same direction as the airflow (forward smolder). While the igniter was energized (during the first 400 s of the experiment), the forced airflow velocity was approximately 0.1 mm/s. The igniter was de-energized at 400 s, at which time the airflow was increased to its nominal value of 5 mm/s. Boundary conditions are implemented as described below.

At $z = \delta$, where the forced flow is introduced, the composition of the volatiles is specified:

$$Y_j|_{z=\delta} = Y_{j\delta} \quad (75a)$$

The oxygen and nitrogen mass fractions are, respectively, 0.23 and 0.77. At $z = 0$ (flow outlet) a high Peclet number is assumed:

$$\left. \frac{\partial Y_j}{\partial z} \right|_{z=0} = 0 \quad (75b)$$

The temperature at $z = \delta$ (where the igniter is located) is specified to equal the experimentally measured igniter temperature:

$$T|_{z=\delta} = T_{ign}(t) \quad (76a)$$

At $z = 0$, the conductive heat flux balances convective and radiative losses:

$$-k \left. \frac{\partial T}{\partial z} \right|_{z=0} = h_c(T|_{z=0} - T_\infty) - \bar{\epsilon}(T^4|_{z=0} - T_\infty^4) \quad (76b)$$

where h_c is 10 W/m²K and T_∞ is 300 K. The pressure gradient at $z = \delta$ is set to give the desired mass flux:

$$-\frac{\bar{K}}{\bar{v}} \left. \frac{\partial P}{\partial z} \right|_{z=\delta} = \dot{m}''_\delta(t) \quad (77a)$$

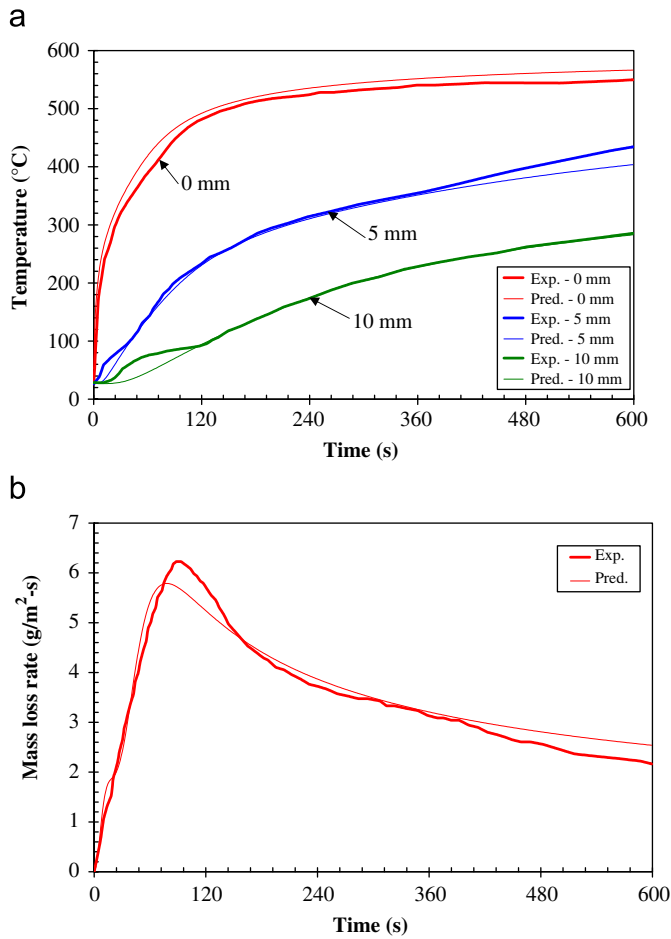


Fig. 11. Comparison of model calculations using optimized input parameters and experimental data for pyrolysis of white pine at 40 kW/m² irradiance in nitrogen. (a) Temperature; (b) Mass loss rate.

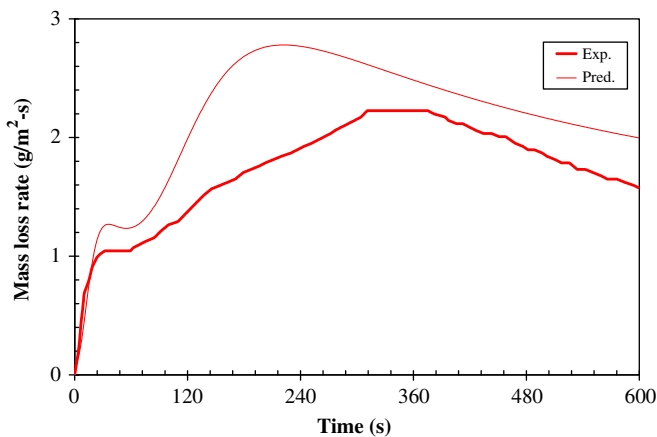


Fig. 12. Comparison of modeled mass loss rate and experimental data for pyrolysis of white pine at 25 kW/m² irradiance in nitrogen.

Table 8

Condensed phase parameters for intumescent coating simulations.

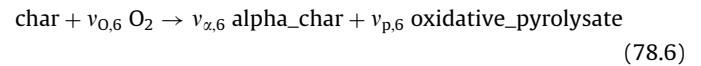
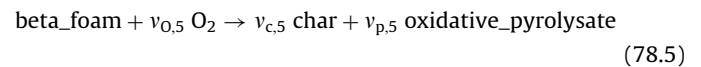
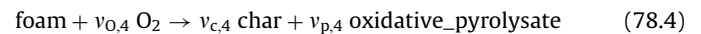
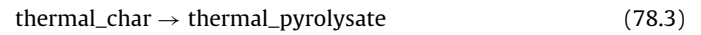
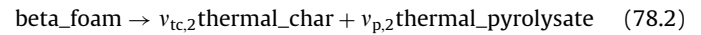
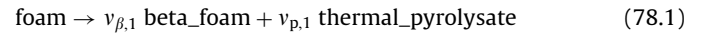
| <i>i</i> | Name | k_0 (W/m K) | n_k (–) | ρ_0 (kg/m ³) | n_p (–) | c_0 (J/kg K) | n_c (–) | ε (–) | κ (m ^{–1}) | γ (m) | K (m ²) | ρ_{s0} (kg/m ³) |
|----------|----------------|---------------|-----------|-------------------------------|-----------|----------------|-----------|-------------------|-----------------------------|-----------------------|-----------------------|----------------------------------|
| 1 | virgin_coating | 0.176 | 0.352 | 1000 | 0 | 1600 | 0 | 0.85 | ∞ | 0 | 1×10^{-11} | 1010 |
| 2 | char | 0.041 | 0.441 | 17.4 | 0 | 1640 | 0 | 0.91 | ∞ | 3.00×10^{-3} | 1×10^{-10} | 1010 |
| 3 | ash | 0.020 | 0.503 | 2.9 | 0 | 1723 | 0 | 0.92 | ∞ | 4.98×10^{-3} | 1×10^{-9} | 1010 |
| 4 | steel | 56.0 | –0.330 | 7833 | 0 | 465 | 0 | 0.90 | ∞ | 0 | 1×10^{-10} | 7834 |

(–) denotes dimensionless.

The forced mass flux is 0.1 g/m²s for the first 400 s, ramping linearly to 5.8 g/m²s between 400 and 410 s. The pressure at $z = 0$ is set to atmospheric (101.3 kPa):

$$P|_{z=0} = P_{\infty} \quad (77b)$$

The experiment is simulated here using a seven-step reaction mechanism developed by Dodd et al. [34]. Five condensed phase species are tracked (foam, beta_foam, thermal_char, char, and alpha_char):



The reaction rate of reactions (78.3) and (78.7) are insignificant except near the transition from smolder to flaming. Four gaseous species are tracked for this particular simulation: (1) thermal_pyrolysate, (2) nitrogen, (3) oxygen, and (4) oxidative_pyrolysate. Model parameters, based on Dodd et al. [34], are given in Tables 10–12.

To account for radial heat losses, a volumetric heat loss coefficient of 25 W/m³K is applied, i.e. a source term of $-25(T - T_{\infty})$ W/m³ is added to the condensed phase energy equation. The value of 25 W/m³K was estimated by matching the slope of the predicted thermocouple temperatures after the smolder front has passed to the experimental data.

Fig. 16a shows the calculated temperature profiles at several different times. The smolder wave propagates from right to left (the igniter is located at $z = 14$ cm) with a velocity of approximately 0.25 mm/s. The airflow is also from right to left, i.e. the airflow is introduced at $z = 14$ cm. Calculated peak smolder temperatures are approximately 450 °C. Fig. 16b shows profiles of oxygen mass fraction inside the pore space. Comparison of Fig. 16b with Fig. 16a indicates that oxygen is consumed at the smolder front (where peak temperatures are the highest).

Fig. 17 compares the Gpyro temperature calculations with the experimental data, and it can be seen that the agreement is reasonable.

7. Concluding remarks

This paper presents the mathematical formulation of Gpyro, a generalized pyrolysis model for combustible solids. The model's

Table 9
Reaction parameters for intumescent coatings simulations.

| k | From | To | χ (–) | ΔH_{sol} (J/kg) | ΔH_{vol} (J/kg) | Z (s ^{–1}) | E (kJ/mol) | n (–) | n_{O_2} (–) |
|---|----------------|------|------------|-------------------------|-------------------------|------------------------|--------------|---------|---------------|
| 1 | virgin_coating | char | 0.66 | 0 | 5.77×10^5 | 1.44×10^{13} | 160.3 | 6.02 | 0 |
| 2 | char | ash | 1 | 0 | -3.09×10^5 | 7.05×10^5 | 171.5 | 3.53 | 0 |

(–) denotes dimensionless.

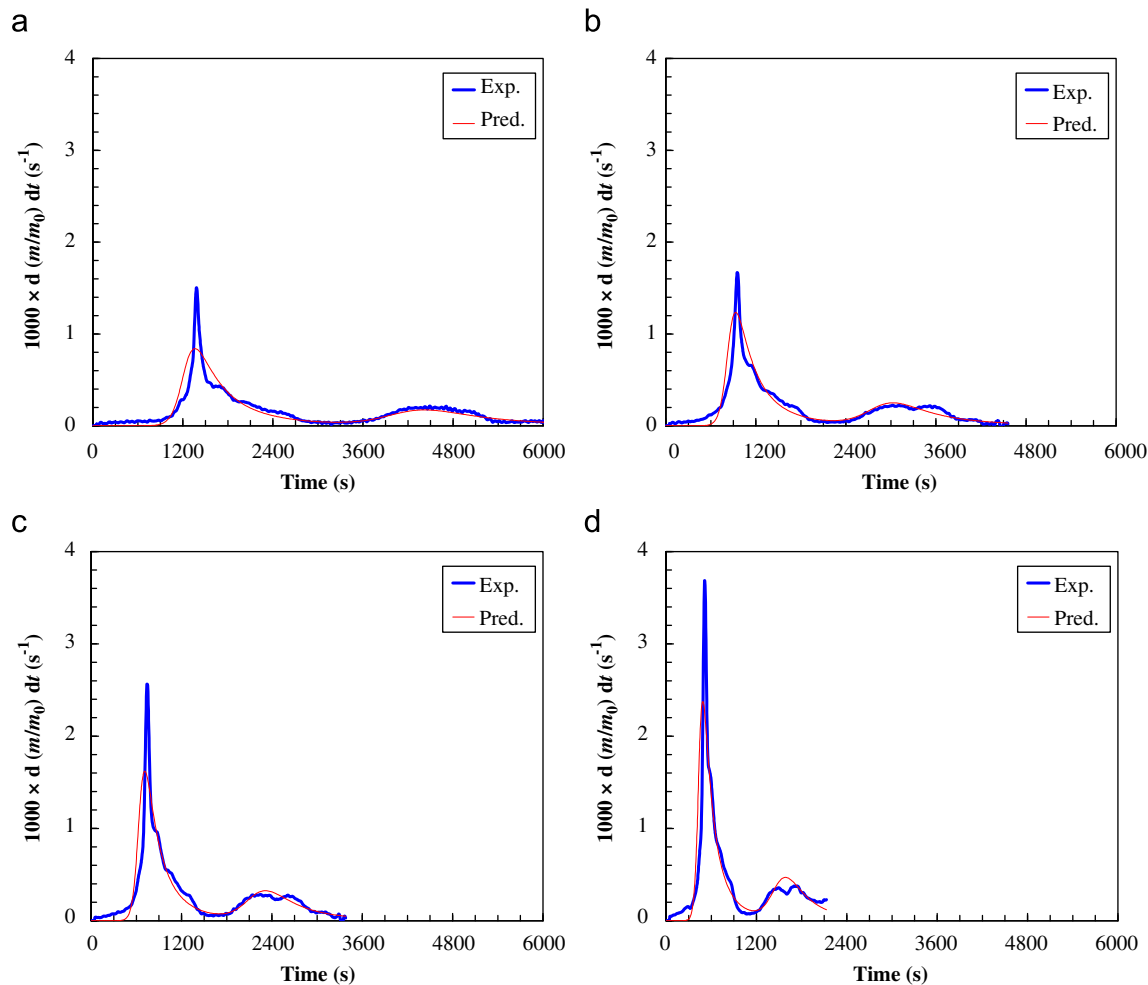


Fig. 13. Comparison of experimentally measured [32] and modeled differential thermogravimetric curves of an intumescent coating. Material A from Reference [32] in nitrogen atmosphere at several heating rates: (a) 10 °C/min; (b) 15 °C/min; (c) 20 °C/min; (d) 30 °C/min.

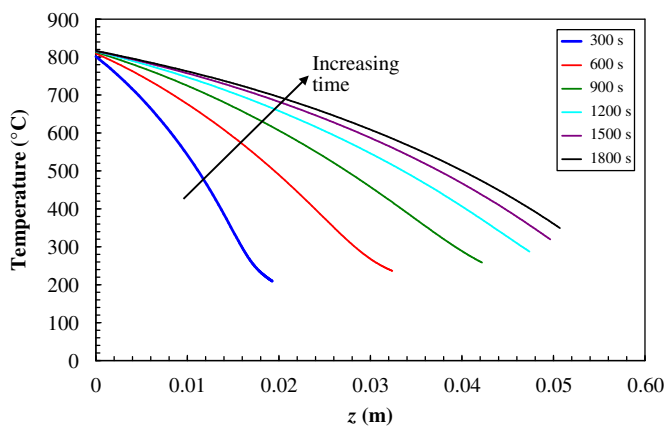


Fig. 14. Calculated temperature profiles during irradiation of intumescent coating (material A from Ref. [32]) at 90 kW/m² in reduced O₂ atmosphere.

flexibility is demonstrated by simulating four experiments: thermo-oxidative decomposition of a noncharring polymer (PMMA), thermal pyrolysis of a charring solid (white pine), gasification and swelling of an intumescent coating, and propagation of a smolder wave in polyurethane foam. Since most required model input parameters cannot be easily measured, they are estimated by genetic algorithm optimization [15,16] from bench-scale fire tests and thermogravimetry. Generally, good agreement between model calculations and experimental data is obtained, particularly when one considers that Gpyro was not developed to simulate a particular material or experimental configuration. This suggests that Gpyro adequately describes the pyrolysis of a variety of fuels when provided with adequate material property estimates.

It is not yet possible to separate pyrolysis model “validation” from material property estimation. Current pyrolysis models, including Gpyro, contain submodels for physical phenomena that require as input material properties that cannot be easily

measured and therefore must be *inferred* from experimental data, introducing considerable uncertainty. It is therefore felt that rather than adding new physical phenomena or more complex

reaction mechanisms to existing pyrolysis models, future research should focus on material property estimation. Work is needed primarily in three areas:

- (1) Development of improved pyrolysis model property estimation algorithms. To date, genetic algorithms have been applied, but these are not necessarily the best algorithms for material property estimation. It is likely that hybrid methods based on genetic algorithms, simulated annealing, and gradient-based search are more efficient than optimization algorithms currently in use.
- (2) Development of a customized fire test that is designed specifically to provide pyrolysis model input parameters. Existing bench-scale fire tests such as the cone calorimeter measure a material's overall reaction to fire and provide a means to estimate effective flammability properties (thermal inertia, ignition temperature, etc.). However, they were never intended as a means to estimate the parameters needed for numerical pyrolysis modeling. Consequently, nuances of existing bench-scale flammability tests make them less than ideal for pyrolysis model material property estimation.
- (3) Development of a “best practices” guide to determining material properties for pyrolysis modeling. At the time of writing, NIST has sponsored development of such a guide and initial work is underway.

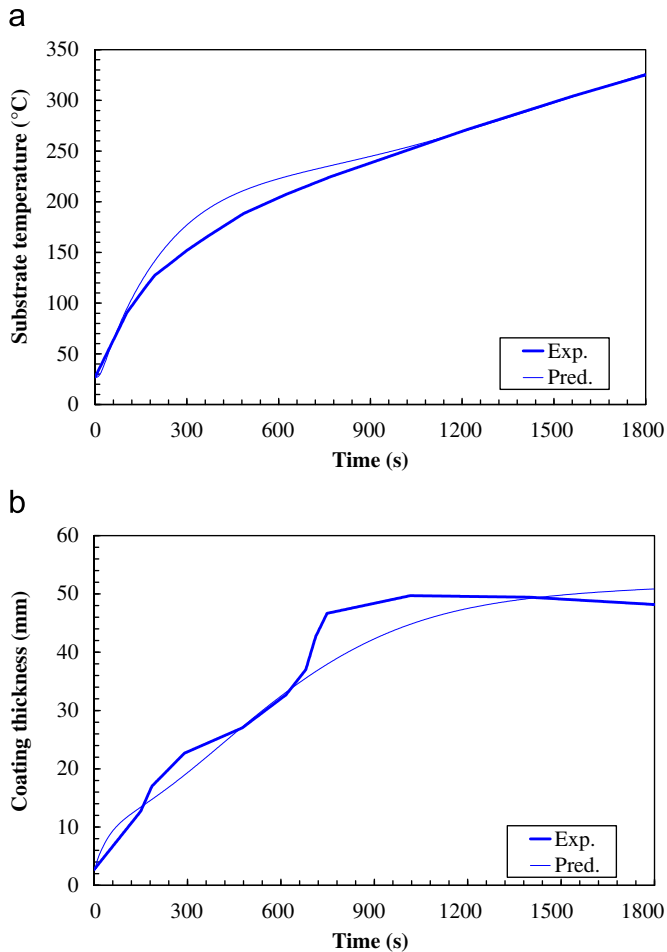


Fig. 15. Comparison of experimental cone calorimeter data [32] and model calculations for intumescent coating. Material A from Reference [32] irradiated at 90 kW/m² in reduced O₂ atmosphere. (a) Substrate temperature; (b) Thickness.

Table 10

Condensed phase parameters for smolder simulations.

| <i>i</i> | Name | k_0 (W/mK) | n_k (–) | ρ_0 (kg/m³) | n_p (–) | c_0 (J/kgK) | n_c (–) | ε (–) | κ (m⁻¹) | γ (m) | K (m²) | ρ_{s0} (kg/m³) |
|----------|--------------|--------------|-----------|------------------|-----------|---------------|-----------|-------------------|----------------|--------------|----------------------|---------------------|
| 1 | foam | 0.05 | 1.6 | 26.5 | 0 | 1760 | 0.7 | 1 | ∞ | 0.001 | 5.2×10^{-9} | 900 |
| 2 | beta_foam | 0.05 | 1.6 | 18.0 | 0 | 1760 | 0.7 | 1 | ∞ | 0.001 | 1.0×10^{-8} | 900 |
| 3 | thermal_char | 0.05 | 1.6 | 1.1 | 0 | 1760 | 0.7 | 1 | ∞ | 0.001 | 3.0×10^{-8} | 900 |
| 4 | char | 0.05 | 1.6 | 10.0 | 0 | 1760 | 0.7 | 1 | ∞ | 0.001 | 3.0×10^{-8} | 900 |
| 5 | alpha_char | 0.05 | 1.6 | 2.4 | 0 | 1760 | 0.7 | 1 | ∞ | 0.001 | 3.0×10^{-8} | 900 |

(–) denotes dimensionless.

Table 11

Reaction parameters for smolder simulations.

| <i>k</i> | From | To | χ (–) | ΔH_{sol} (J/kg) | ΔH_{vol} (J/kg) | Z (s⁻¹) | E (kJ/mol) | n (–) | n_{O_2} (–) |
|----------|--------------|--------------|------------|-------------------------|-------------------------|-----------------------|--------------|---------|---------------|
| 1 | foam | beta_foam | 1 | 4.00×10^4 | 4.00×10^4 | 3.16×10^{18} | 227.0 | 0.80 | 0 |
| 2 | beta_foam | thermal_char | 1 | 7.50×10^5 | 7.50×10^5 | 1.29×10^{10} | 146.5 | 1.25 | 0 |
| 3 | thermal_char | gases | 1 | -2.50×10^6 | -2.50×10^6 | 8.24×10^8 | 173.3 | 0.92 | 0 |
| 4 | foam | char | 1 | -1.50×10^6 | -1.50×10^6 | 1.37×10^{15} | 188.0 | 0.48 | 1 |
| 5 | beta_foam | char | 1 | -1.60×10^6 | -1.60×10^6 | 1.00×10^{16} | 200.0 | 0.52 | 1 |
| 6 | char | alpha_char | 1 | -2.50×10^6 | -2.50×10^6 | 1.00×10^{15} | 201.0 | 1.30 | 1 |
| 7 | alpha_char | gases | 1 | -2.50×10^6 | -2.50×10^6 | 4.25×10^8 | 153.0 | 1.61 | 1 |

(–) denotes dimensionless.

Table 12

Gaseous yields for smolder simulations (only nonzero yields shown).

| <i>j</i> | <i>k</i> | | | | | | |
|--------------------------|----------|---|---|-------|-------|-------|-------|
| | 1 | 2 | 3 | 4 | 5 | 6 | 7 |
| 1 (thermal_pyrolysate) | 1 | 1 | 1 | | | | |
| 2 (nitrogen) | | | | | | | |
| 3 (oxygen) | | | | –0.30 | –0.40 | –1.50 | –1.50 |
| 4 (oxidative_pyrolysate) | | | | 1.30 | 1.40 | 2.50 | |
| 5 (products) | | | | | | | 2.50 |

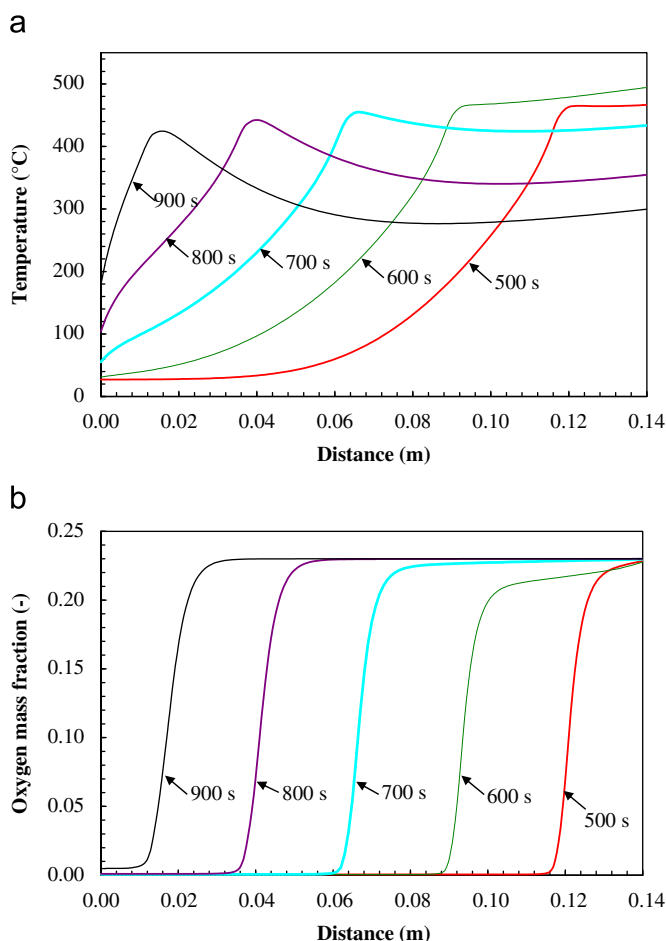


Fig. 16. Calculated profiles in smoldering polyurethane foam at several different times. Airflow is 5 mm/s, (a) temperature and (b) oxygen mass fraction inside voids.

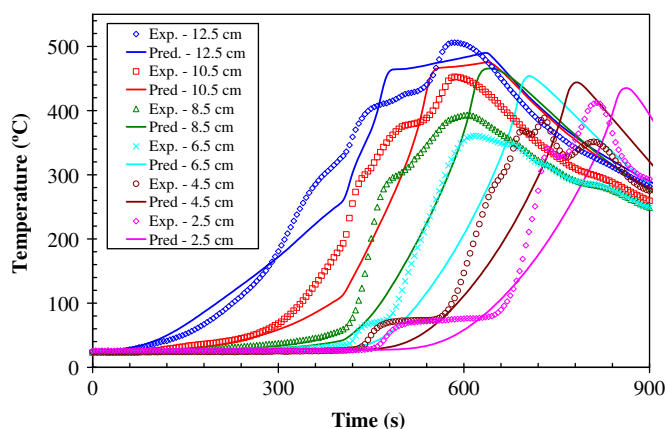


Fig. 17. Comparison of experimentally measured [34] and modeled temperature at several locations in a polyurethane foam cylinder smoldering in microgravity. 5 mm/s airflow velocity.

Acknowledgments

This work was supported by the National Science Foundation under Grant 0730556 and the NASA Graduate Student Researcher Program under Grant NNC-04HA08H. The authors thank G. Griffin for providing the experimental data for the intumescent coating in spreadsheet form. Many discussions critical to the model

development process were held with G. Rein, J. Torero, J. Quintiere, and N. Dembsy, and we would like to thank them for their insight and suggestions. Two anonymous reviewers provided detailed comments that helped strengthen this paper.

References

- [1] C. Di Blasi, Modeling and simulation of combustion processes of charring and non-charring solid fuels, *Progress in Energy and Combustion Science* 19 (1993) 71–104.
- [2] T. Kashiwagi, Polymer combustion and flammability—role of the condensed phase, *Proceedings of the Combustion Institute* 25 (1994) 1423–1437.
- [3] A.C. Fernandez-Pello, The solid phase, in: G. Cox (Ed.), *Combustion Fundamentals of Fire*, Academic Press, New York, 1995, pp. 31–100.
- [4] C. Di Blasi, The state of the art of transport models for charring solid degradation, *Polymer International* 49 (2000) 1133–1146.
- [5] R.E. Lyon, M.L. Janssens, Polymer flammability, DOT/FAA/AR-05/14, 2005.
- [6] B. Moghtaderi, The state-of-the-art in pyrolysis modeling of lignocellulosic solid fuels, *Fire and Materials* 30 (2006) 1–34.
- [7] C. Lautenberger, A.C. Fernandez-Pello, Pyrolysis modeling, thermal decomposition, and transport processes in combustible solids, in: M. Faghri, B. Sunden (Eds.), *Transport Phenomena in Fires*, WIT Press, 2008, pp. 209–259.
- [8] C. Di Blasi, Modeling chemical and physical processes of wood and biomass pyrolysis, *Progress in Energy and Combustion Science* 34 (2008) 47–90.
- [9] J.E.J. Staggs, Modeling thermal degradation of polymers using single-step first-order kinetics, *Fire Safety Journal* 32 (1999) 17–34.
- [10] J.T. Kuo, C.L. Hsi, Pyrolysis and ignition of single wooden spheres heated in high-temperature streams of air, *Combustion and Flame* 142 (2005) 401–412.
- [11] C. Di Blasi, Modeling the effects of high radiative heat fluxes on intumescent material decomposition, *Journal of Analytical and Applied Pyrolysis* 71 (2004) 721–737.
- [12] S.V. Leach, G. Rein, J.L. Ellzey, O.A. Ezekoye, Kinetic and fuel property effects on forward smoldering combustion, *Combustion and Flame* 120 (2000) 346–358.
- [13] <<http://code.google.com/p/gpyro>>.
- [14] C.W. Lautenberger, A generalized pyrolysis model for combustible solids, Ph.D. Dissertation, Department of Mechanical Engineering, University of California, Berkeley, CA, December 2007. <<http://repositories.cdlib.org/cpl/fs/LautenbergerPhD>>.
- [15] C. Lautenberger, G. Rein, A.C. Fernandez-Pello, The application of a genetic algorithm to estimate material properties for fire modeling from bench-scale fire test data, *Fire Safety Journal* 41 (2006) 204–214.
- [16] G. Rein, C. Lautenberger, A.C. Fernandez-Pello, J.L. Torero, D.L. Urban, Application of genetic algorithms and thermogravimetry to determine the kinetics of polyurethane foam in smoldering combustion, *Combustion and Flame* 146 (2006) 95–108.
- [17] R.B. Bird, W.E. Stewart, E.N. Lightfoot, *Transport Phenomena*, Wiley, New York, 1960.
- [18] S.V. Patankar, *Numerical Heat Transfer and Fluid Flow*, Hemisphere Publishing Corporation, New York, 1980.
- [19] A.F. Mills, *Mass Transfer*, Prentice-Hall, Upper Saddle River, NJ, 2001, p. 161.
- [20] T. Kashiwagi, T.J. Ohlemiller, A study of oxygen effects on nonflaming transient gasification of PMMA and PE during thermal irradiation, *Proceedings of the Combustion Institute* 19 (1982) 815–823.
- [21] J.-W. Kwon, N.A. Dembsy, C.W. Lautenberger, Evaluation of FDS V.4: upward flame spread, *Fire Technology* 43 (2007) 255–284.
- [22] T. Steinhilber, Evaluation of the thermophysical properties of poly(methylmethacrylate): a reference material for the development of a flammability test for micro-gravity environments, M.S. Thesis, University of Maryland, Department of Fire Protection Engineering, 1999.
- [23] S.S. Manohar, A.K. Kulkarni, S.T. Thynell, In-depth absorption of externally incident radiation in nongray media, *Journal of Heat Transfer* 117 (1995) 146–151.
- [24] J.R. Hallman, J.R. Welker, C.M. Sliepcevich, Polymer surface reflectance-absorbance characteristics, *Polymer Engineering and Science* 14 (1974) 717–723.
- [25] H. Zhang, *Fire-safe polymers and polymer composites*, DOT/FAA/AR-04/11, 2004.
- [26] J.D. Peterson, S. Vyazovkin, C.A. Wight, Kinetic study of stabilizing effect of oxygen on thermal degradation of poly(methylmethacrylate), *Journal of Physical Chemistry B* 103 (1999) 8087–8092.
- [27] T.J. Ohlemiller, T. Kashiwagi, K. Werner, Wood gasification at fire level heat fluxes, *Combustion and Flame* 69 (1987) 155–170.
- [28] T. Kashiwagi, T.J. Ohlemiller, K. Werner, Effects of external radiant flux and ambient oxygen concentration on nonflaming gasification rates and evolved products of white pine, *Combustion and Flame* 69 (1987) 331–345.
- [29] F. Jia, E.R. Galea, M.K. Patel, Numerical simulation of the mass loss process in pyrolyzing char materials, *Fire and Materials* 23 (1999) 71–78.
- [30] W.G. Weng, Y. Hasemi, W.C. Fan, Predicting the pyrolysis of wood considering char oxidation under different ambient oxygen concentrations, *Combustion and Flame* 145 (2006) 723–729.

- [31] C. Lautenberger, A.C. Fernandez-Pello, A model for the oxidative pyrolysis of wood, *Combustion and Flame*, in press, doi:10.1016/j.combustflame/2009.04.001.
- [32] G.J. Griffin, A.D. Bicknell, T.J. Brown, Studies on the effect of atmospheric oxygen content on the thermal resistance of intumescent, fire-retardant coatings, *Journal of Fire Sciences* 23 (2005) 303–328.
- [33] A. Bar-Ilan, G. Rein, A.C. Fernandez-Pello, J.L. Torero, D.L. Urban, Forced forward smoldering experiments in microgravity, *Experimental Thermal and Fluid Science* 28 (2004) 743–751.
- [34] A.B. Dodd, C. Lautenberger, A.C. Fernandez-Pello, Numerical examination of two-dimensional smolder structure in polyurethane foam, *Proceedings of the Combustion Institute* 32 (2009) 2497–2504.